

EUROPEAN ORGANISATION FOR NUCLEAR RESEARCH (CERN)



October 31, 2023

Report from the NA61/SHINE experiment at the CERN SPS

The NA61/SHINE Collaboration

This document reports on the status and plans of the NA61/SHINE experiment at the CERN SPS as of November 2023. The document refers to the proposal SPSC-P-330.

CERN-SPSC-2023-030 / SPSC-SR-336
01/11/2023



Contents

1. Introduction	6
2. Data-taking summary	6
2.1. Pb ion physics run, autumn 2022	6
2.2. Neutrino-related physics run, summer 2023	7
2.3. Pb ion physics run, autumn 2023	7
3. Facility status	8
4. Software and calibration status	10
4.1. Software	10
4.2. Calibration	13
5. New results	20
5.1. New results for strong interaction physics	20
5.2. New results for neutrino and cosmic-ray physics	33
6. Beam request for 2024 and plans for 2025	42
6.1. Beam request for 2024	42
6.2. Plans for measurements in 2025	43
7. Summary	43
A. Nuclear fragmentation measurements for Galactic cosmic-ray physics	47
A.1. Motivation	47
A.2. Impact of measurements by NA61/SHINE	48
B. High-statistics measurements of $p+p$ interactions for cosmic-ray and strong interaction physics	52

The NA61/SHINE Collaboration

H. Adhikary ¹¹, P. Adrich ¹³, K.K. Allison ²⁴, N. Amin ⁴, E.V. Andronov ²⁰, I.-C. Arsene ¹⁰, M. Bajda ¹⁴, Y. Balkova ¹⁶, D. Battaglia ²³, A. Bazgir ¹¹, S. Bhosale ¹², M. Bielewicz ¹³, A. Blondel ³, M. Bogomilov ², Y. Bondar ¹¹, A. Brandin²⁰, W. Bryliński ¹⁹, J. Brzychczyk ¹⁴, M. Buryakov ²⁰, A.F. Camino²⁶, M. Ćirković ²¹, M. Csanád ⁶, J. Cybowska ¹⁹, T. Czopowicz ¹¹, C. Dalmazzone ³, N. Davis ¹², A. Dmitriev ²⁰, P. von Doetinchem ²⁵, W. Dominik ¹⁷, J. Dumarchez ³, R. Engel ⁴, G.A. Feofilov ²⁰, L. Fields ²³, Z. Fodor ^{5,18}, M. Friend ⁷, M. Gaździcki ¹¹, O. Golosov ²⁰, V. Golovatyuk ²⁰, M. Golubeva ²⁰, K. Grebieszko ¹⁹, F. Guber ²⁰, S.N. Igolkin²⁰, S. Ilieva ², A. Ivashkin ²⁰, A. Izvestnyy ²⁰, N. Kargin²⁰, N. Karpushkin ²⁰, E. Kashirin ²⁰, M. Kielbowicz ¹², V.A. Kireyeu ²⁰, R. Kolesnikov ²⁰, D. Kolev ², Y. Koshio⁸, V.N. Kovalenko ²⁰, S. Kowalski ¹⁶, B. Kozłowski ¹⁹, A. Krasnoperov ²⁰, W. Kucewicz ¹⁵, M. Kuchowicz ¹⁸, M. Kuich ¹⁷, A. Kurepin ²⁰, A. László ⁵, M. Lewicki ¹⁸, G. Lykasov ²⁰, V.V. Lyubushkin ²⁰, M. Maćkowiak-Pawłowska ¹⁹, Z. Majka ¹⁴, A. Makhnev ²⁰, B. Maksiak ¹³, A.I. Malakhov ²⁰, A. Marcinek ¹², A.D. Marino ²⁴, H.-J. Mathes ⁴, T. Matulewicz ¹⁷, V. Matveev ²⁰, G.L. Melkumov ²⁰, A. Merzlaya ¹⁰, Ł. Mik ¹⁵, S. Morozov ²⁰, Y. Nagai ⁶, T. Nakadaira ⁷, M. Naskręt ¹⁸, S. Nishimori ⁷, A. Olivier ²³, V. Ozvenchuk ¹², O. Panova ¹¹, V. Paolone ²⁶, O. Petukhov ²⁰, I. Pidhurskyi ¹¹, R. Płaneta ¹⁴, P. Podlaski ¹⁷, B.A. Popov ^{20,3}, B. Pórfy ^{5,6}, D.S. Prokhorova ²⁰, D. Pszczel ¹³, S. Puławski ¹⁶, J. Puzović^{21†}, R. Renfordt ¹⁶, L. Ren ²⁴, V.Z. Reyna Ortiz ¹¹, D. Röhrich⁹, E. Rondio ¹³, M. Roth ⁴, Ł. Rozpłochowski ¹², B.T. Rumberger ²⁴, M. Rumyantsev ²⁰, A. Rustamov ¹, M. Rybczynski ¹¹, A. Rybicki ¹², K. Sakashita ⁷, K. Schmidt ¹⁶, A.Yu. Seryakov ²⁰, P. Seyboth ¹¹, U.A. Shah ¹¹, Y. Shiraishi⁸, A. Shukla ²⁵, M. Słodkowski ¹⁹, P. Staszal ¹⁴, G. Stefanek ¹¹, J. Stepaniak ¹³, M. Strikhanov²⁰, Ł. Świdorski ¹³, J. Szewiński ¹³, R. Szukiewicz ¹⁸, A. Taranenko ²⁰, A. Tefelska ¹⁹, D. Tefelski ¹⁹, V. Tereshchenko²⁰, R. Tsenov ², L. Turko ¹⁸, T.S. Tveter ¹⁰, M. Unger ⁴, M. Urbaniak ¹⁶, F.F. Valiev ²⁰, D. Veberič ⁴, V.V. Vechernin ²⁰, O. Vitiuk ¹⁸, V. Volkov ²⁰, A. Wickremasinghe ²², K. Witek ¹⁵, K. Wójcik ¹⁶, O. Wyszzyński ¹¹, A. Zaitsev ²⁰, E. Zherebtsova ¹⁸, E.D. Zimmerman ²⁴, A. Zviagina ²⁰, and R. Zwaska ²²

[†] *deceased*

¹ National Nuclear Research Center, Baku, Azerbaijan

² Faculty of Physics, University of Sofia, Sofia, Bulgaria

³ LPNHE, Sorbonne University, CNRS/IN2P3, Paris, France

⁴ Karlsruhe Institute of Technology, Karlsruhe, Germany

⁵ HUN-REN Wigner Research Centre for Physics, Budapest, Hungary

⁶ Eötvös Loránd University, Budapest, Hungary

⁷ Institute for Particle and Nuclear Studies, Tsukuba, Japan

⁸ Okayama University, Japan

⁹ University of Bergen, Bergen, Norway

¹⁰ University of Oslo, Oslo, Norway

¹¹ Jan Kochanowski University, Kielce, Poland

¹² Institute of Nuclear Physics, Polish Academy of Sciences, Cracow, Poland

¹³ National Centre for Nuclear Research, Warsaw, Poland

¹⁴ Jagiellonian University, Cracow, Poland

¹⁵ AGH - University of Science and Technology, Cracow, Poland

¹⁶ University of Silesia, Katowice, Poland

¹⁷ University of Warsaw, Warsaw, Poland

¹⁸ University of Wrocław, Wrocław, Poland

¹⁹ Warsaw University of Technology, Warsaw, Poland

²⁰ Affiliated with an institution covered by a co-operation agreement with CERN

²¹ University of Belgrade, Belgrade, Serbia

²² Fermilab, Batavia, USA

²³ University of Notre Dame, Notre Dame, USA

²⁴ University of Colorado, Boulder, USA

²⁵ University of Hawaii at Manoa, Honolulu, USA

²⁶ University of Pittsburgh, Pittsburgh, USA

The NA61/SHINE Limited Members

T. Antićić ¹, S. Bordoni⁷, A. Bravar⁶, N. Charitonidis⁷, P. Christakoglou², G. Christodoulou⁷, A. De Roeck⁷, F. Diakonos², S.J. Dolan⁷, R.A. Fernandez⁷, K.J. Floethner⁷, A. Kapoyannis², U. Kose⁷, M.O. Kuttan³, O. Linnyk³, L. Munteanu⁷, C. Mussolini⁷, A.D. Panagiotou², J. Pawlowski³, W. Rauch⁴, L. Scharenberg⁷, S. Schramm³, J. Steinheimer-Froschauer³, H. Stoecker³, H. Ströbele⁵, T. Šušā ¹, A. Toia ⁵, M. Vassiliou², C.F. Vilela⁷, and K. Zhou³

¹ Ruđer Bošković Institute, Zagreb, Croatia

² University of Athens, Athens, Greece

³ Frankfurt Institute for Advanced Studies,
Frankfurt, Germany

⁴ Fachhochschule Frankfurt, Frankfurt, Germany

⁵ University of Frankfurt, Frankfurt, Germany

⁶ University of Geneva, Geneva, Switzerland

⁷ CERN, Geneva, Switzerland

1. Introduction

This annual report presents the status and plans of the NA61/SHINE experiment [1] at the CERN SPS. The report refers to the period November 2022 – October 2023.

The document is organized as follows. A summary of the 2022 and 2023 data-taking campaigns is given in Section 2. The facility status is given in Section 3. Software and calibration upgrades are summarized in Section 4. New results are presented in Section 5. The beam request for 2024 and plans for data taking in 2025 are presented in Section 6. The summary in Section 7 closes the paper.

An addendum to the NA61/SHINE proposal was submitted by the NA61/SHINE Collaboration to the SPS Committee in the reported period [2]. It requests light-ion beams during the Run 4 period for the study of the QGP-fireball onset.

Following a request from the SPSC referees, we provide more details on the physics impact of nuclear fragmentation measurements with NA61/SHINE in Appendix A. Additional arguments for considered measurements for cosmic-ray and strong interaction physics with the proton beam are provided in Appendix B.

2. Data-taking summary

Since the last Status Report [3], data collection has occurred in three primary periods: the Pb beam run in autumn 2022, the neutrino-related run in summer 2023, and the Pb beam run in autumn 2023.

2.1. Pb ion physics run, autumn 2022

In 2022, the Pb beam at a momentum of $150A \text{ GeV}/c$ was delivered to the NA61/SHINE experiment on the 16th of November. After one week of setup, the production data taking started with a 3 mm lead target, providing 6% interaction probability. The data were taken with the unbiased interaction T2 trigger (identified interaction) and beam T1 trigger (identified beam) scaled down by a factor of 100. The sub-systems used in this data-taking were: Beam Position Detector (BPD-3), Time Projection Chambers (TPCs), the Trigger and Data Acquisition system (TDAQ), the upgraded Vertex Detector (VD), the Time-of-Flight-Left (ToF-L), and the Main and Forward Projectile Spectator Detectors (MPSD, FPSD).

The total number of interaction trigger events collected during one week of the production data-taking period amounts to 50 million. This includes about 30 million Pb+Pb collisions. It was the first NA61/SHINE measurement with a lead ion beam performed after the hardware upgrade during the Long Shutdown 2 (LS2).

2.2. Neutrino-related physics run, summer 2023

NA61/SHINE collected data with secondary hadrons for six weeks in July and August 2023. The full detector was operational for most of the data collection period, except for the silicon beam position detectors, which were replaced successfully by delay wire chambers borrowed from the CERN Beams Department (BE). The first four weeks of the period were devoted to 60 GeV/ c K^+ +C interactions, and the remaining two weeks to 120 GeV/ c proton interactions on Ti and C. A total of 383 million events were collected during the summer run, twenty times the size of the largest neutrino-related data sets collected before LS2. The new high-rate DAQ provided the opportunity not only to take much higher signal statistics than in the past but also to take special runs to address systematic effects.

The K^+ +C interaction is essential for understanding secondary interactions in long primary targets used in neutrino beams. For this measurement, data collection with the new DAQ was limited by the low ($\sim 4\%$) fraction of kaons in the beam. A total of 86.2 million events were collected with the target in. However, because our trigger cannot distinguish interactions from the more common beam kaon decays, we estimate that fewer than half of the events are true kaon interactions. Kaon decays can also be a background at the analysis level, so a larger-than-normal amount of target-out running (51.5 million events) was performed to have statistics for background subtraction. An additional 9.6 million events were collected with the target out and full magnetic field to measure the beam particle composition.

An additional program of 120 GeV/ c interaction studies was conducted in the final two weeks of the run. This period's main goal was to measure interaction cross-sections on grade 5 titanium, an important structural component of neutrino beam target assemblies. A combination of efficient triggering and very good accelerator performance allowed us to collect 102.5 million p +Ti events, above the goal for this process, as well as an opportunistic run of 75.5 million p +C events that will allow us to improve significantly on the precision of the 2016–2017 measurements we published this year (Sec. 5.2). Eighteen million events were collected with 120 GeV/ c protons and target out.

Due to some cryogenic system failures, the superconducting vertex magnets were inoperative for several days of the run period. We used this time to collect ancillary data sets for measuring total production and interaction cross-sections on materials. This information is useful for constraining systematic uncertainties in our measurements of differential cross-sections and is a publishable physics measurement. We recorded magnet-off data for p +Ti, π^+ +Ti, and K^+ +Ti at 60 GeV/ c ; and p +C at 90 and 120 GeV/ c . About 26.6 million events were taken with targets in and 12.5 with targets out.

2.3. Pb ion physics run, autumn 2023

On September 30th, 2023, the Pb beam at a momentum of 150A GeV/ c was delivered to the NA61/SHINE experiment. After five days of setup, the production data taking started with a 3 mm lead target, providing 6% interaction probability. The data were taken with the minimum bias interaction T2 trigger and with beam T1 trigger scaled down by a factor of 100, resulting in the data sample consisting of around 8% of T1 (beam) triggers and 92% of T2

(interaction) triggers. The sub-systems used in this data-taking were Beam Position Detectors (BPD-1 and BPD-3), Time Projection Chambers (VTPCs and MTPCs), the Trigger and Data Acquisition system (TDAQ), the upgraded Vertex Detector (VD), the Time-of-Flight-Left (ToF-L), and the Forward Projectile Spectator Detector (FPSD).

The data-taking rate with the upgraded NA61/SHINE detector is 1.2 kHz over 8.5 s SPS spill in 2023. Upgrades of the detector, combined with optimization of the SPS slow extraction, resulted in increased data-taking efficiency with respect to 2018 Pb data-taking by a factor of about 30. The total number of interaction trigger events collected during four calendar weeks of the Pb period amounts to about 300 million. This includes about 150 million Pb+Pb collisions. Thus, with 30 million collisions taken in 2022, NA61/SHINE has recorded about 180 million collisions for open charm physics. The goal of 500 million events should be reached, assuming in total of seven weeks of the Pb beam in 2024 and 2025 with the planned increased efficiency of the interaction trigger.

Request concerning future scheduling of ion runs. The SPSC recommended and the Research Board approved two and four weeks of the Pb beam in 2022 and 2023, respectively. This, however, did not account for a significant planned reduction of the allocated beam time due to the LHC filling and the operation of the machines with protons for AWAKE. The reduction due to the LHC filling is unavoidable, but it changes yearly, and we request to account for it in the SPSC beam-time allocation. In 2023, the SPSC allocated calendar beam time was reduced by the LHC filling from 28 days to 23 days of the effective beam time. Further, the effective beam time was reduced by operating the machines with protons for AWAKE during the Pb period. This can be avoided. In 2023, the operation with protons reduced the effective Pb beam for NA61/SHINE to 21 days. Consequently, in 2023, the effective beam time for NA61/SHINE amounted to about 75% of the allocated by SPSC calendar time.

In conclusion, we request the SPSC to allocate to NA61/SHINE the effective ion beam time (the time relevant for physics) and the calendar time (the time relevant for logistics). This should greatly help in the SPSC and NA61/SHINE planning of physics output.

3. Facility status

During the Long Shutdown 2 at CERN (2019–2021), the NA61/SHINE spectrometer was significantly modified (the layout is presented in Fig. 1). The upgrade was motivated by the charm and neutrino programs, both of which require a tenfold increase of the data-taking rate to about 1 kHz. The charm program also requires doubling the phase-space coverage of the Vertex Detector. The neutrino physics run in 2022 proved that the primary goal of the upgrade was achieved. The maximum data-taking rate reached 1.6 kHz (for low multiplicity events), much higher than the assumed 1 kHz. The Pb run was performed in fall 2022 and 2023, again showing the very good performance of the upgraded detector. In 2023 the data-taking rate was about 1.2 kHz.

Control over the value and time evolution of the anode currents of the Sense Wires is of utmost importance for the health of the TPCs. Up to 2023, only old, human-readable nanoampere meters were installed in NA61/SHINE for such monitoring purposes. Therefore, an

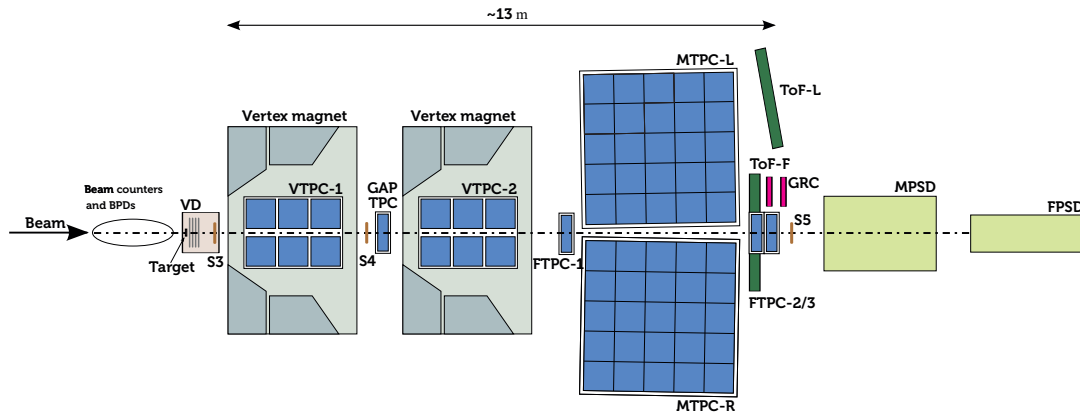


Figure 1: The layout of the NA61/SHINE detector.

effort was made in order to obtain a nanoampmeter system, capable of monitoring 96 channels in the dynamic range 1–5000 nA, with positive or negative polarities, at a 10 Hz read-out rate, communicating via a simple Ethernet read-out interface module. The system consists of 2 crates, each hosting 8 measurement cards, each card capable of reading 6 high voltage (HV) channels up to ± 2000 V. By now, they are fully integrated into the NA61/SHINE Detector Control System (DCS). Figure 2 shows their performance: the left panel shows the photo of the two nanoamper measurement crates with some of the HV channels connected, the top right panel shows the read-out current time-value series in the DCS during ramping individual HV channels showing negligible cross-leak currents, the bottom right panel shows the read-out current time-value series during data taking showing the in-spill and out-of-spill currents.



Figure 2: *Left:* The photo of the new nanoamp meter crates. *Right top:* The read-out current time-value series in the DCS during ramping individual HV channels, showing negligible cross-leak currents. *Right bottom:* The read-out current time-value series during data taking, showing the in-spill and out-of-spill VTPC-1 anode currents, as an example.

The very considerable effort the Collaboration invested in the detector upgrade opens new options for physics measurements and ensures the operation of the NA61/SHINE experiment for the next few years.

4. Software and calibration status

4.1. Software

During the reporting period software work has been steadily progressing. Main efforts were dedicated to support reconstruction, calibration, and quality monitoring of the data collected with the upgraded detector. Some key developers left the Collaboration, but responsibilities and knowledge were successfully transferred without losses to the overall work efficiency. This resulted in readiness for data taking in summer and autumn. The next section covers the progress on the framework and general issues, as well as lists miscellaneous changes associated with specific sub-systems, while further sections discuss larger sub-system-specific projects.

4.1.1. SHINE framework

Since the previous report, work is ongoing on a new regular software release. This longer-than-standard time between releases is caused by work on the structure of the calibration database (which has to be synchronized with the software) and revision of core framework components. The former is associated, on the one hand, with the inclusion of new detectors and, on the other, with housekeeping for old systems where we already have a clear idea of how information should be organized. Similarly, over the previous years, we have developed a better understanding of what is needed regarding the core SHINE components. All this is meant to make it easier for new developers to join the work and for the users to utilize the software.

While the work goes on, one patch release was issued supporting MC production for pre-LS2 data, and five so-called release candidates were prepared. The latter are installations on `cvmfs` to support data taking and calibration for the newly collected data, but are not kept compatible with the developing calibration database structure beyond their temporary use.

Some of the changes to the framework, as well as minor sub-system-specific changes are listed below.

- (i) One of the key components that were revised are managers. They are classes that are responsible for reading in detector-related information from the database and other sources. Their interfaces were re-worked and associated documentation was improved to make it clear how managers should be implemented, tested, and used.
- (ii) Long-standing problems with dependencies in the build system were solved preventing random crashes that confused newcomers.

- (iii) We now have nightly builds of the doxygen documentation for the master branch of SHINE available on a documentation web page.
- (iv) We moved back to an official version of GEANT4 from our customization of GEANT4 10.7 after the necessary improvements appeared in GEANT4 11.1.
- (v) Associated with the above we moved to C++17 standard, as well as to the gcc 12 compiler on lxplus/lxbatch and GitLab CI with support from the CERN EP-SFT group.
- (vi) Missing information was added for pre-LS2 time of flight detectors, the detector description software was revised and streamlined. The new module was implemented to provide expected hit positions of tracks in ToF walls.
- (vii) The software to parse and calibrate the DRS4 data was prepared.
- (viii) Silicon Beam Position Detectors and the new Forward Time-of-Flight detector were integrated in the software. Work is ongoing on the support for MRPC time of flight detectors and extended Projectile Spectator Detector.

Apart from the above, we continue improving the native tracking and continue its validation against the legacy clients.

4.1.2. GRC

In order to constantly monitor and measure the drift velocity in the TPC chambers, a new segmented reference detector, the GRC (Geometry Reference Chamber) was developed and installed during the LS2. The GRC chambers are, as of now, placed downstream of MTPC-L. Several software infrastructures needed to be developed in order to use this new equipment. In the SHINE offline software, the following parts were developed: raw event containers, parser from DAQ format to raw event format, raw event display in the `eventBrowser`, detector description, IO managers filling the detector description, raw event monitoring module, reconstructed event containers, reconstruction modules, data quality assessment modules, and finally the calibration module actually using the GRC data for the drift velocity estimation.

4.1.3. Vertex Detector software

The upgrade of the Vertex Detector [4,5], which was performed from 2020 to 2022 (based on the ALPIDE-sensors-based modules (called *staves*) developed within the ALICE-ITS project [6]), required an upgrade to the Vertex Detector track reconstruction software. The schematic layout of staves with indicated active sensors is drawn in red (Jura arm) and green (Saleve arm) in Fig. 3.

The software upgrade was performed sequentially for each reconstruction SHINE module, which was used for its predecessor, a Small Acceptance Vertex Detector (SAVD). The entire reconstruction chain retained the same structure, however, we invented the naming convention of the new modules by adding “Al” in front of the original SAVD name, referring to the ALPIDE sensors used.

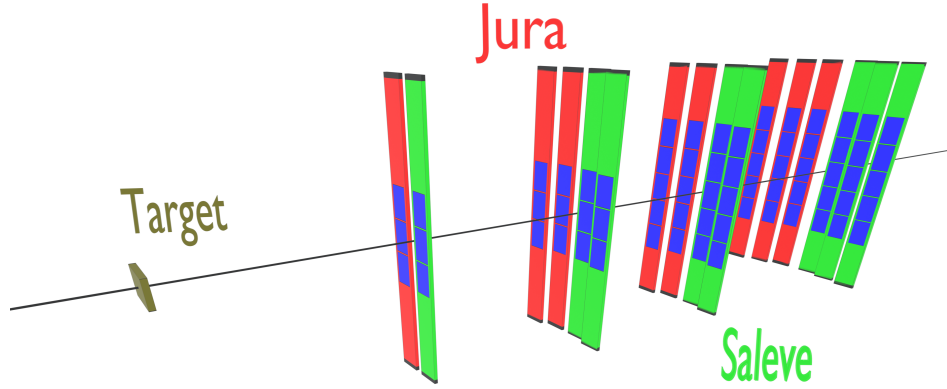


Figure 3: The schematic layout of the used sensors (blue rectangles) located on staves. The corresponding arms (Jura and Saleve) are marked in red and green [4].

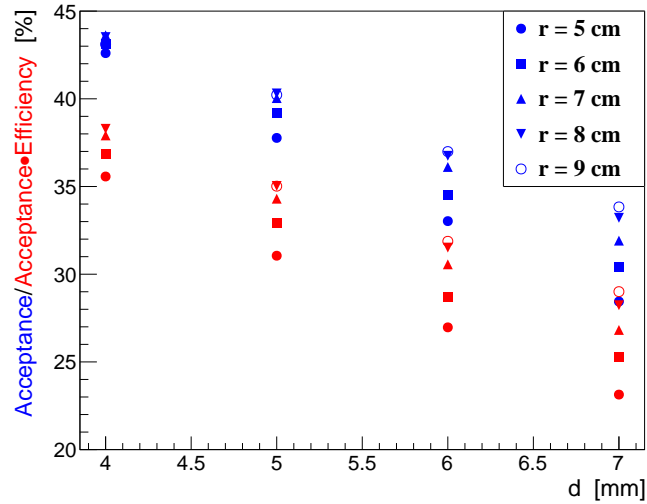


Figure 4: The integrated acceptance (blue) and acceptance multiplied by reconstruction efficiencies (red) of D^0 mesons for all considered cases.

The upgraded reconstruction modules were tested and optimized based on simulations of collisions of a Pb beam with a momentum of $150A \text{ GeV}/c$ on a 3 mm thick Pb target. The following efforts were dedicated to establish the acceptance and reconstruction efficiency of D^0 charmed mesons [4] for the reconstructed sensor geometry (see Section 4.2.2). This was done for different distances d (gap) between the arms Jura and Saleve based on the layout of the first station and for different distances r between the 3 mm target Pb position to the first station. The D^0 meson acceptance and reconstruction efficiencies for all considered cases are presented in Fig. 4.

4.1.4. DAQ and new on-line QA

During data-taking periods in November 2022 and summer 2023 the offline quality-assessment (QA) was assuring good quality of data. The files with recorded data were being transferred to CTA or EOS, and a notification to the OfflineQA service was sent to process them immediately in a pool of 2000 HTCondor cores devoted exclusively for this purpose. The resulting reports on data quality were discussed on a daily basis.

For the summer 2023 data-taking period, a new online quality-assessment service was prepared in order to have proper data monitoring in real time.

Online analysis of the data is performed by a series of processes running the ShineOffline reconstruction software. Copies of events obtained by the TDAQ are distributed between a set of "event servers", from where they are fetched by the aforementioned ShineOffline instances. Produced QA data is then accumulated by a dedicated service that performs additional QA where higher statistics is required and, finally, writes the QA data to a disk. An overview of the QA data is done via a dedicated web application.

The upgrade consisted of the introduction of the centralized collector for the QA data and the development of the new front-end application. Both are directed on simplifying the maintenance of the system:

- (i) Centralized collector for the QA data introduces a convenient place for any auxiliary monitoring code.
- (ii) Display contents of the new front-end application is fully configurable via *JSON* to simplify adaptation to changes in QA data contents.

Moreover, the upgraded online QA is capable to process every single event recorded by the TDAQ, improving the overall quality of the QA.

4.2. Calibration

Calibration activities and upgrades performed during the last year are the following:

(A) Concerning Pb+Pb collisions at $150A$ GeV/ c collected in 2022

- (i) Kr calibration data collected in November 2022 were carefully analyzed, and gain factors for TPC pads were obtained and included in the database.
- (ii) The Wiener filter of the shape of the signals from the new TPC electronics was prepared and applied to the data. It filtered out the elongated part of the signals. As a result, the clusters have a more rounded shape.
- (iii) The TPC pad-by-pad time constants (t_0) were obtained by the analysis of electronic pulse signals.
- (iv) The positions and tilt angles were extracted using a new alignment procedure that uses field-off data.

- (v) The drift velocity calibration was done using standard Δy vs y alignment plots using a new GRC instead of the previously used ToF-L counter.
 - (vi) The trigger latency time correction $t0Corr$ and position misalignment y_0 were obtained by varying drift velocity, and using Δy vs y plots.
 - (vii) Local residual corrections (cluster positions relative to tracks) were applied for every TPC.
 - (viii) The database structure and dedicated managers were created for Vertex Detector data.
 - (ix) The preliminary merging algorithm and software for tracks from Vertex Detector and TPCs were prepared and used.
- (B) Concerning 2022 neutrino-related data
- (i) Conversion of ADC counts to voltages (voltage calibration) was done for DRS4 boards of the ToF-F detector.
 - (ii) Local and global time calibration and the time synchronization of boards were done for DRS4 boards of the ToF-F detector.
 - (iii) BPD-GEM detectors were calibrated for 2022 neutrino-related data.
- (C) Concerning data collected prior to detector upgrade
- (i) The final calibration of ToF-L/R counters was done for Xe+La and Pb+Pb data samples using native calibration software.
 - (ii) Data managers were written and used for SHINE processing of ToF-L/R correction factors from the database.
 - (iii) The final mass productions were prepared for all Xe+La data samples, and Pb+Pb collisions at $13A$ and $30A$ GeV/ c .
 - (iv) The BPD position residual corrections and BPD strip gains calibration factors were obtained for $p+p$ events collected at 400 GeV/ c .
 - (v) TPC calibration, i.e. drift velocity (v_{drift}), time constants, and geometrical corrections, was done for $p+p$ at 400 GeV/ c data sample using the newest SHINE calibration software.

4.2.1. TPC calibration for 2022 Pb+Pb data

Since during the LS2, the TPC Front-End Electronics (FEE) were replaced by the former ALICE FEEs, a methodology for a new gain table became necessary. By now, there is a standard technique for equalizing the pad-by-pad gains, using the spectrum of radioactive krypton decays. A software tool for analyzing such Kr data was developed and commissioned. During the Kr data taking, a random trigger was used, and the appearing TPC clusters were reconstructed. The spectrum of the cluster total charges reflects the lines of the Kr energy spectrum, and a pad-by-pad gain correction table was calculated in order to equalize the highest energy Kr peak position across the TPC chambers. For small pads, charge leakage to

adjacent pads was of concern, as for these pads, the single-pad total charge resolution was by nature relatively limited. In order to mitigate this issue, not only the position of the main Kr peak was detected for each pad, but also the trailing slope of the main Kr peak was involved in the calibration-analysis. Using this technique, the pad-by-pad relative gains were equalized throughout the TPC chambers; the corresponding calibration task was completed (see also Status Report 2022 [3] for example plots).

When the TPC drift time sampling is started, the actual start time of the drift sampling can have a slight relative latency for each pad, called pad-by-pad t_0 correction. If not corrected for, the adjacent pads can have a slight phase shift, which in turn translates to a slight degradation of the position resolution in the drift direction. In order to mitigate this effect, an electronic pulser-based calibration procedure was developed: an electronic pulser pulses the Field Wires of the TPCs simultaneously, and the pulse shape as seen by each pad is reconstructed. Their tiny relative phase is then extracted with a software analyzer tool, providing the pad-by-pad t_0 correction table; see Fig. 5 as an example. The corresponding tool was developed and deployed this year, and the corresponding calibration task was completed.

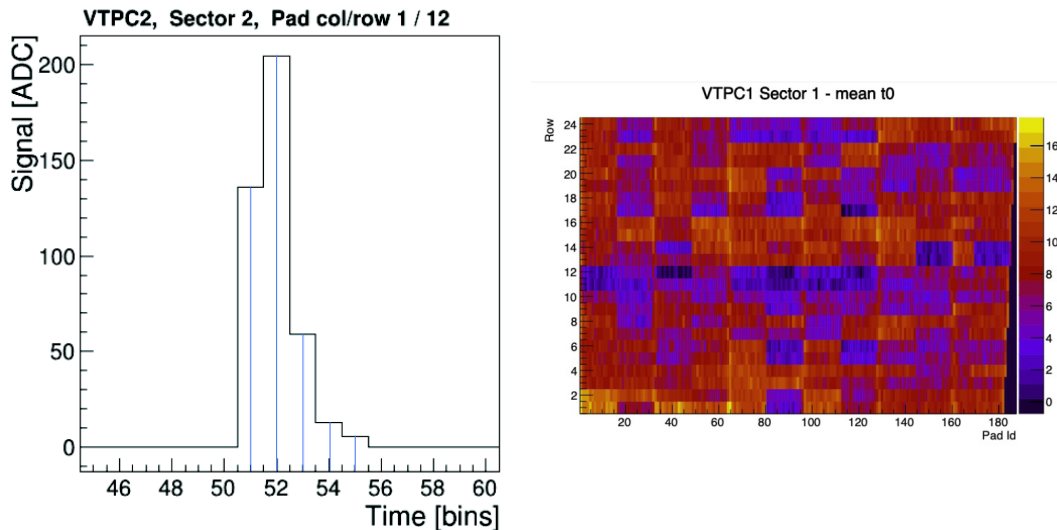


Figure 5: *Left:* Typical electronic pulse shape as seen by a TPC pad FEE channel. *Right:* The t_0 map of a Sector1 of VTPC-1 (units in nanoseconds).

The signal formation in a TPC chamber is dominated by the signal of ions formed in the amplification avalanche process at the Sense Wires. The response on the pads are actually the mirror charges of the positive ion cloud. Since despite of the high field at the Sense Wires, the drift of the ions is relatively slow, this results in a power-law-like tail in the response of TPC pads as a function of drift time. These long tails, if not corrected for, would significantly bias the drift coordinate estimate of clusters and, moreover, would prolongate the clusters in the drift direction, which would cause unnecessary cluster overlaps. In order to mitigate the issue, a calibration tool was developed and deployed, which records the mean response function belonging to healthy track clusters, and from this, in combination with the known noise level, calculates an optimal Wiener filter. Then, during reconstruction, the TPC pad time trace raw data is filtered with such a Wiener filter profile before clusterization. The Wiener filter is calculated for each TPC Sector. A demonstration of the effect of the Wiener

filter is shown in Fig. 6.

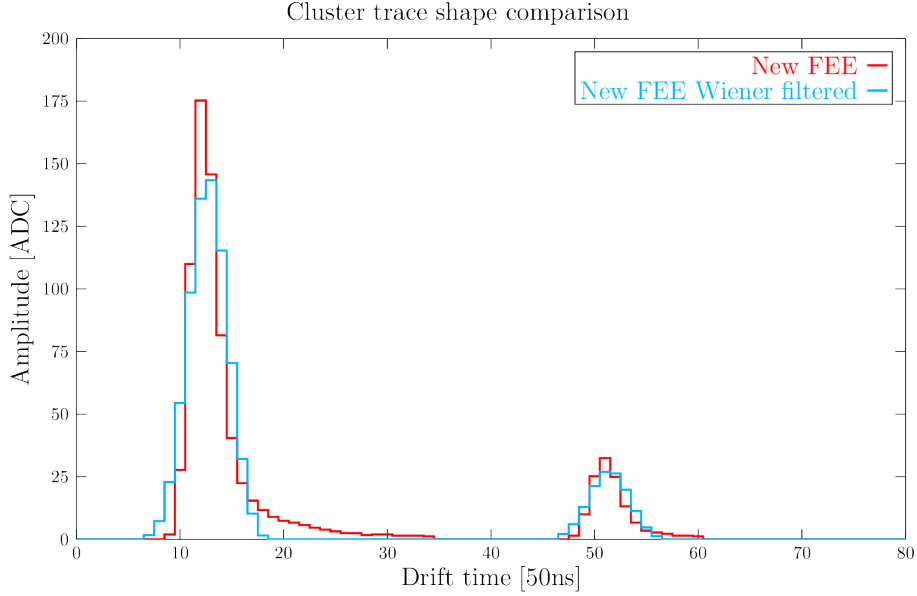


Figure 6: TPC track cluster time traces with and without the application of the newly developed Wiener filtering procedure.

One of the most sensitive parameters of the TPC system is the estimate for the actual in-situ drift velocity, which is also slowly changing as a function of wall-clock time on the scale of 10 minutes. In order to make this estimate rather direct and accurate, a specific new segmented detector was built and installed downstream of the MTPC-L chamber. The idea is to have an explicit length reference scale for the drift coordinate of MTPC-L. This is done by the already mentioned GRC detector which is implemented as two 40 cm (horizontal) x 120 cm (vertical, i.e. drift direction) cartesian readout multi-Wire proportional chambers (MWPCs). The upstream chamber is used along its full acceptance for low multiplicity runs, whereas the downstream one has a narrowed horizontal acceptance in order to eliminate the cartesian ambiguity for high multiplicity collisions. The principle of the drift velocity calibration is based on the comparison of the extrapolated TPC track drift coordinate to the GRC hits. Whenever the assumed drift velocity during reconstruction is inaccurate, the slope of the drift coordinate mismatch (Δy) versus the drift coordinate (y) as measured by the GRC, will give the drift velocity correction factor by means of the calibration equation $\Delta y = \left(\frac{1}{v_{DriftCorr}} - 1 \right) y + (\text{offset from the displacement of the chambers, etc})$. Here, $v_{DriftCorr} := \frac{v_{drift,true}}{v_{drift,assumed}}$. In this way, the in-situ MTPC-L drift velocity correction factor can be determined from data, in about 5–10 minutes of wall-clock time windows, which is enough for following the drift velocity changes caused by the slow change of the ambient parameters, such as air pressure. An example of such Δy vs y fit is shown in Fig. 7. The other chambers are calibrated successively against each other, using the already calibrated TPCs as geometry reference chambers in the process (MTPC-L \rightarrow VTPC-2, and then VTPC-2 \rightarrow VTPC-1 and VTPC-2 \rightarrow MTPC-R).

A complication in the above procedure is that the imperfection of the TPC chamber alignment gives sizable systematics to the drift velocity estimate using the above method. The

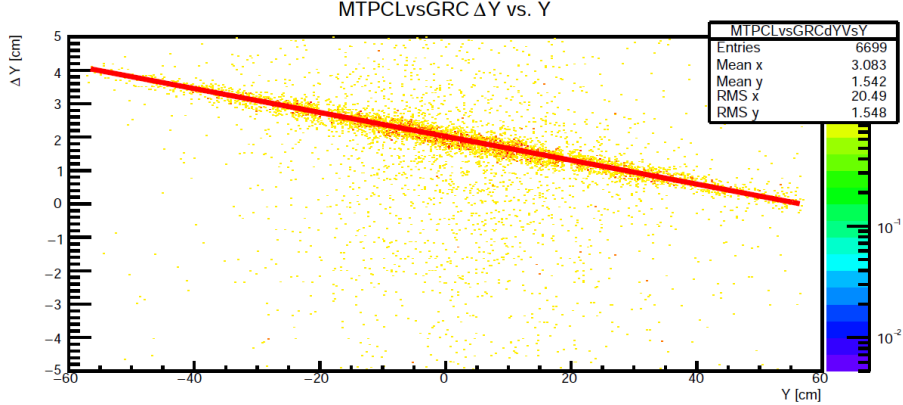


Figure 7: Example for the extraction of the drift velocity correction from the Δy vs y plot. The extrapolated MTPC-L tracks are matched to hits in GRC, and the deviation of the MTPC-L extrapolated positions are plotted against the GRC positions in terms of the drift (y) coordinate. The slope of the deviation plot carries the information on the necessary correction to the drift velocity assumed during the reconstruction. A realistic initial guess is known from the gas composition and the applied drift field.

track-by-track systematics due to alignment imperfections can be seen to be inversely proportional to the z -distance from the main-vertex of the $z = \text{const}$ plane, where the Δy vs y analysis is performed. Therefore, the misalignment gives a small contribution to MTPC-L drift velocity correction, since it is far from the main-vertex, but can give a sizable contribution to the other chambers. Since the VTPCs were moved during LS2, and their new alignment is not known to great precision, a data-based alignment self-calibration method was developed. We take special calibration runs without a magnetic field, in which case the tracks are straight lines. Then, the alignment procedure is inspired by the above Δy vs y analysis: the main-vertex global tracks are split into local track pieces per TPC chamber, they are refitted locally, and the mismatch parameters of the local tracks in adjacent chambers are checked at $z = \text{const}$ reference planes in between. A local straight track segment at a pertinent reference plane is uniquely determined by the z -slopes N_x, N_y and the anchor point coordinates M_x, M_y . Moreover, each chamber has eight unknown alignment parameters: the angular misalignment $\theta_x, \theta_y, \theta_z$, the position misalignment x_0, z_0 along the non-drift coordinates, the drift velocity correction factor $vDriftCorr$, the trigger latency correction $t0Corr$, and the position misalignment y_0 along the drift coordinate. Assuming that one of the chambers is already calibrated (except for t_0 and y_0), the mismatch pattern at the $z = \text{const}$ plane is given to the first order in terms of the calibration parameters by the equation

$$\begin{aligned}
\Delta N_x &= (1 + N_x^2)\theta_y + N_y(N_x\theta_x + \theta_z), \\
\Delta N_y &= N_y^2(\theta_x + \theta_y) + N_y(vDriftCorr - 1) - N_x\theta_z + \theta_x, \\
\Delta M_x &= (\theta_x M_y + \theta_y M_x + z_0)N_x + \theta_y z + \theta_z M_y - x_0, \\
\Delta M_y &= (\theta_x M_y + \theta_y M_x + z_0)N_y + \theta_x z - \theta_z M_x - y_0 \\
&\quad + (M_y - y_{\text{anode,assumed}})(vdriftCorr - 1) - t0Corr v_{\text{drift,assumed}}.
\end{aligned} \tag{1}$$

That is, an imperfection of any of the eight alignment parameters leaves a specific footprint on the mismatch pattern already to the first order. The alignment analysis is performed by first calibrating MTPC-L for drift velocity with the usual Δy vs y method against GRC, and assuming its $\theta_x, \theta_y, \theta_z, x_0, z_0$ parameters to be correct (reference), then analyzing its field-

off mismatch pattern against VTPC-2. For simplification, $|N_y| \approx 0$ tracks are analyzed, for which

$$\begin{aligned}\Delta N_x &= (1 + N_x^2)\theta_y, \\ \Delta N_y &= -N_x\theta_z + \theta_x,\end{aligned}\tag{2}$$

directly provides the angular calibration of VTPC-2. After this is set, one has

$$\Delta M_x = z_0 N_x - x_0\tag{3}$$

for the non-drift coordinate displacement calibration of VTPC-2. This being set, the ordinary Δy vs y analysis based on

$$\Delta M_y = M_y (v_{drift} Corr - 1) + \text{constant offset}\tag{4}$$

yields the drift velocity calibration for VTPC-2. After all this is done, one is left with

$$\Delta M_y = -t_0 Corr v_{drift} - y_0.\tag{5}$$

Taking than data samples where the drift velocity happens to be quite different, one can extract the trigger latency correction $t_0 Corr$ and drift coordinate displacement y_0 of VTPC-2 from the slope and offset of the Δy versus drift velocity analysis. The procedure is then repeated for the further chambers, taking VTPC-2 as a reference. The procedure is demonstrated in Fig. 8.

4.2.2. Software and calibration for the new Vertex Detector

In the calibration procedure of the new VD detector all supplementary constants and parameters, such as the description of the VD geometry, parameters for reconstruction tuning, information on noise pixels, etc., were moved to the common database (DB) used by the ShineOffline software. The introduction of the common DB to the VD software enables us to finally make VD accessible not only for those directly working with it but also to all the other members of our Collaboration. One of the important tasks was the reconstruction of the ALPIDE sensors' positions and rotation angles which was performed for dedicated runs taken with a magnetic field turn-off. This data was taken just before the Pb data-taking period in November 2022. A dedicated procedure was developed based on the minimization of cluster residua for reconstructed tracks fitted with straight lines. The sensor position reconstruction is performed for each arm separately, and the relative positions of arms are then set by looking at offsets in x , y , and z directions between positions of primary vertexes reconstructed separately by Jura and Saleve arms. The distribution of clusters for each station in the x - y plane, which accounts for the reconstructed VD geometry, is shown in Fig. 9.

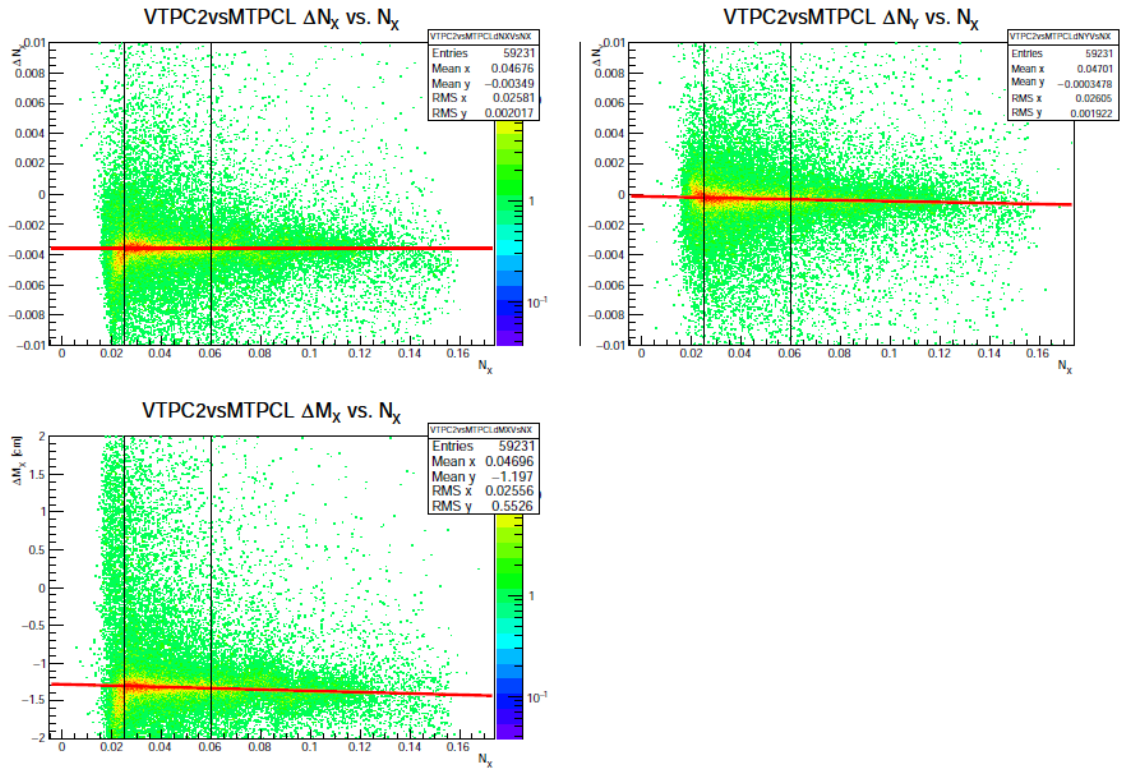


Figure 8: Example for the extraction of the misalignment parameters of the adjacent TPC chambers using field-off track data. In the plot, MTPC-L serves as a reference, and the track parameter mismatch against VTPC-2 pieces is shown along with the corresponding model fit for the extraction of the alignment parameters, see Eqs. (2) and (3). The vertical lines denote the fit region boundaries.

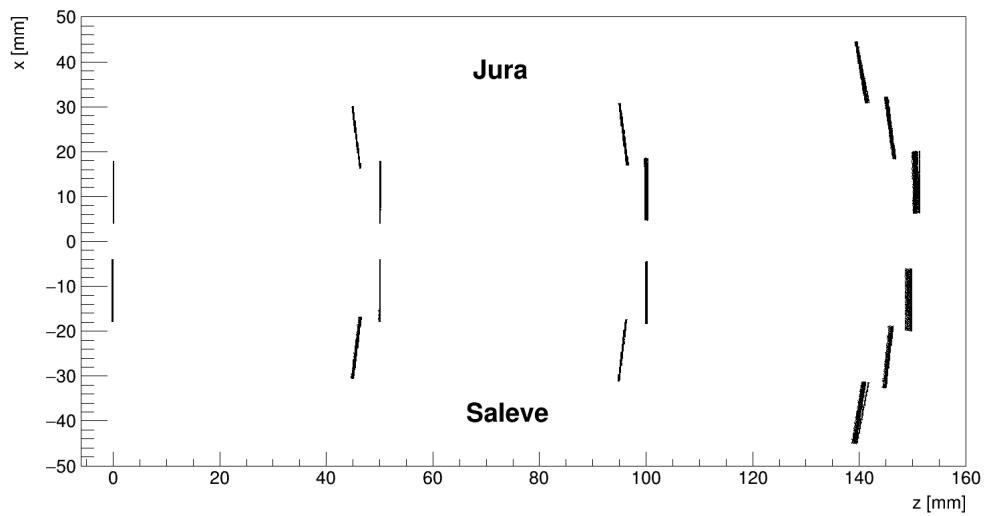


Figure 9: Clusters distribution in the upgraded Vertex Detector.

5. New results

5.1. New results for strong interaction physics

The NA61/SHINE strong interaction program is based on beam momentum scans (13A – 150A/158A GeV/c) with light and intermediate-mass nuclei (from $p+p$ to Xe+La). The main physics goals include searching for the second-order critical end-point in the temperature versus baryo-chemical potential phase diagram and studying the properties of the onset of deconfinement. The program has been extended in recent years by Pb+Pb collisions, where the open charm production and collective effects are studied.

This section summarizes new preliminary and recently published physics results from the program on the physics of strong interactions. The results on spectra and yields, as well as on fluctuations and correlations, are presented. They are labeled according to the NA61/SHINE physics goals, i.e., the study of the onsets of deconfinement (OD) [7] and fireball (OF) [8], the search for the critical point (CP), and others (O).

5.1.1. (O, CP) Published results on femtoscopy analysis in 0–20% central Be+Be collisions at 150A GeV/c

The nature of the quark-hadron transition can be studied via femtoscopy analysis as the investigation of the femtoscopic correlation functions in nucleus-nucleus reactions may reveal the space-time structure of the hadron production source. With the use of Lévy-type sources, we can describe the source parameters (α , λ , and R) as a function of the average transverse mass of the pion pair [9].

The final NA61/SHINE results on femtoscopy analysis in 0–20% central Be+Be collisions at 150A GeV/c were published [10] in *Eur. Phys. J. C*. The 20% most central events were analyzed, and momentum correlations of identified pions were measured. The correlation functions could be described with the assumption of Lévy sources in a statistically acceptable manner, enabling the interpretation of the fit parameters.

The Lévy stability parameter α describes the shape of the source. Furthermore, α was conjectured to be related to one of the critical exponents (the so-called correlation exponent η) and thus may shed light on the location of the critical end-point on the QCD phase diagram [11]. As shown in Fig. 10, our measured α parameter is approximately constant with regards to transverse mass (m_T). The pion-producing source in the 150A GeV/c Be+Be collision appears to be compatible with the Lévy shape assumption, far away from Gaussian and close to Cauchy and not at the CP (corresponding to $\alpha = 2$, $\alpha = 1$, and $\alpha \leq 0.5$, respectively). Our new, final results yield values for α between 0.9 and 1.5, which is significantly lower than preliminary results from 0–10% central Ar+Sc collisions at 150A GeV/c [12].

The correlation strength λ is related to the core-halo ratio, where the core contains pions created primordially or from short-lived resonances, while the halo consists of the decay products of longer-lived resonances. In previous RHIC and SPS results – see e.g. Refs. [13–15] (STAR, PHENIX), Ref. [16] (NA44) or Ref. [17] (NA49) – an intriguing collision energy

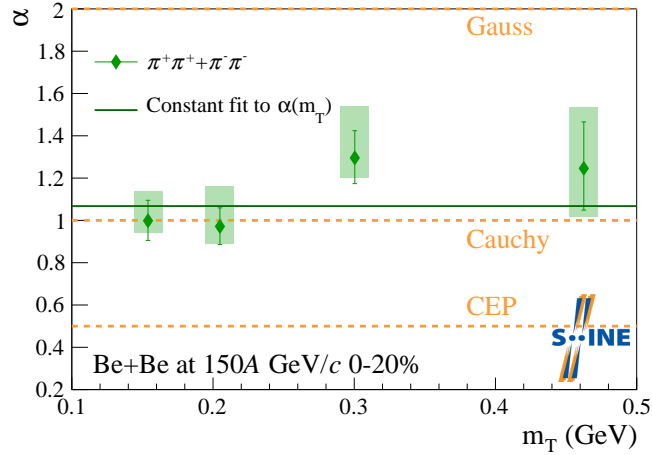


Figure 10: Lévy stability parameter α versus m_T in 0–20% central Be+Be collisions at 150A GeV/c. The three cases for α are marked and shown with dashed lines. Gaussian shape with $\alpha = 2$, Cauchy shape with $\alpha = 1$, and vicinity of the CP (denoted CEP) at $\alpha \leq 0.5$.

dependence of $\lambda(m_T)$ was found: at RHIC, a dip in λ values was observed in the low- m_T region, while no clear dip appeared in case of SPS data.

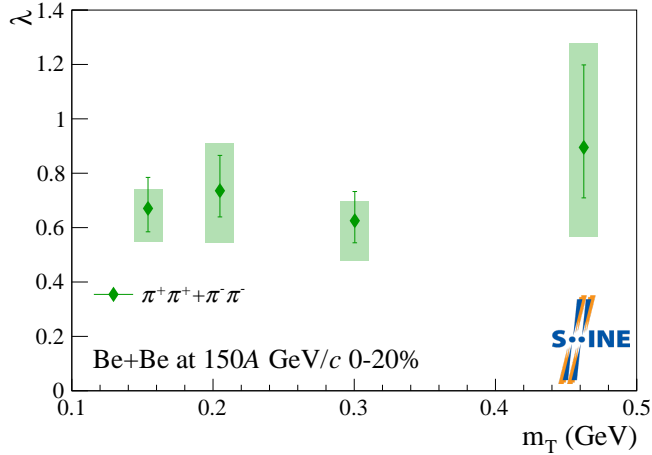


Figure 11: Lévy correlation strength λ versus m_T in 0–20% central Be+Be collisions at 150A GeV/c.

In our results in Fig. 11, we see no significant m_T dependence, similar to NA44, NA49 results, and preliminary results on Ar+Sc measurements of Lévy HBT from NA61/SHINE. This might indicate that the effect of lowering of λ at low- m_T , present at RHIC energies, is “turned off” at the SPS. This requires further study.

The Lévy scale R corresponds to the femtoscopic scale of the system, i.e., the length of homogeneity. From a simple hydro picture, one obtains an $R \propto 1/\sqrt{m_T}$ type of transverse mass dependence, creating a decreasing trend of R in m_T , generally attributed to transverse flow. Our results shown in Fig. 12 indicate that R decreases with m_T , showing a hydro-type of transverse flow effect. This is interesting in particular as we observe the described $R \propto 1/\sqrt{m_T}$, however, one would expect this to show only at $\alpha = 2$ [18]; this phenomenon

was also observed at RHIC [13].

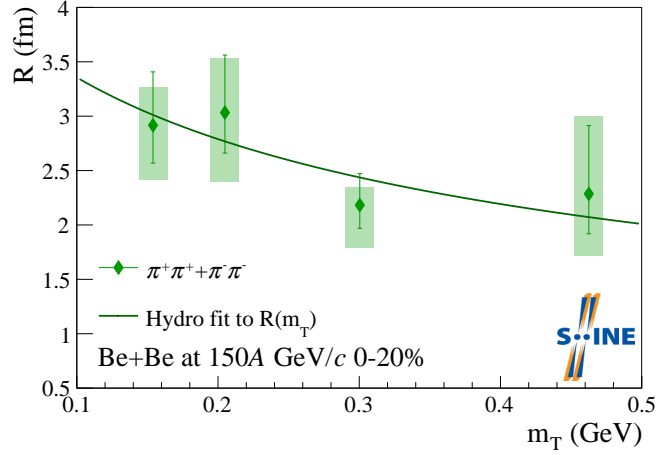


Figure 12: Lévy scale parameter R versus m_T in 0–20% central Be+Be collisions at 150A GeV/c.

5.1.2. (CP) Published results on proton intermittency in Ar+Sc collisions at 150A GeV/c

The final NA61/SHINE results on proton intermittency in different centralities of Ar+Sc collisions at 150A GeV/c were published [19] in *Eur. Phys. J. C*. The example plots from the paper are discussed below.

An example of the dependence of the second scaled factorial moment of proton multiplicity distribution for 0–20% central Ar+Sc collisions at 150A GeV/c on the number of subdivisions in cumulative transverse momentum space is shown in the left panel of Fig. 13. Closed circles indicate the experimental data. For comparison, corresponding results for mixed events (open triangles) and the EPOS1.99 [20,21] model (open squares) are also shown.

The right panel of Fig. 13 presents p-values obtained from the comparison of $F_2(M)$ values for the Power-law Model with different parameters (power-law exponent and fraction of correlated protons) with the corresponding experimental results. For the calculation, statistical uncertainties from the model with similar statistics to the data were used.

The intermittency index ϕ_2 for an infinite system at the QCD critical point is expected to be equal to $\phi_2 = 5/6$, assuming that the latter belongs to the 3-D Ising universality class. If this value is set as the power-law exponent of the Power-law Model, the NA61/SHINE data on central Ar+Sc collisions at 150A GeV/c exclude fractions of correlated protons larger than about 0.1%.

5.1.3. (OD, OF) Final (submitted to *Eur. Phys. J. C*) results on π^\pm , K^\pm , p , and \bar{p} production in 0–10% central Ar+Sc collisions at 13A–150A GeV/c

The final results on π^+ , π^- , K^+ , K^- , p and \bar{p} spectra and yields in 0–10% central Ar+Sc collisions at 13A–150A GeV/c were submitted for publication and are available in Ref. [22]. Spectra presented in the publication include: i) K^\pm , π^\pm and p at 13A–150A GeV/c, ii) \bar{p} at

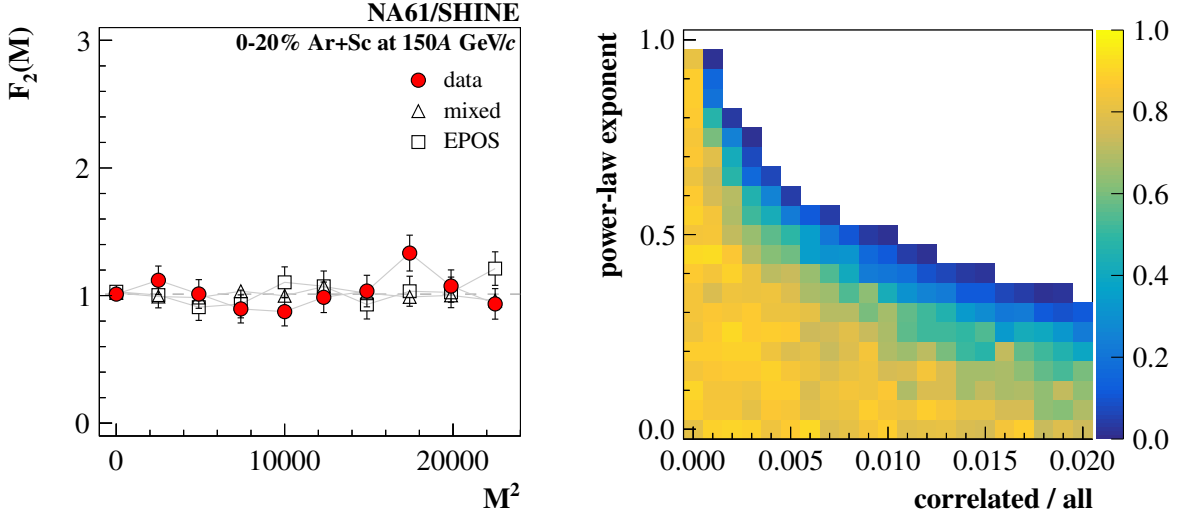


Figure 13: *Left:* Results on the dependence of the second-order scaled factorial moment of proton multiplicity distribution on the number of subdivisions in cumulative transverse momentum space for 0–20% Ar+Sc collisions at 150A GeV/c. Only statistical uncertainties are indicated. *Right:* Exclusion plot, the p-values, for the Power-law Model parameters – the fraction of correlated protons and the power-law exponent. The white areas correspond to p-values less than 1%.

30A–150A GeV/c. Results are obtained in a combined acceptance of dE/dx and $tof - dE/dx$ particle identification methods.

The NA61/SHINE measurements of the inverse slope parameter T at mid-rapidity (*step* plot) in the 10% most central Ar+Sc collision are shown versus collision energy for K^+ and K^- in Fig. 14. The energy dependence of the inverse slope parameter of p_T spectra in central Ar+Sc collisions exhibits a characteristic plateau in the SPS energy range, visible prominently in Pb+Pb data. The Ar+Sc values of the T parameter are located slightly below Pb+Pb, yet still significantly higher than Be+Be and $p+p$. The most recent results for Xe+La data at 150A GeV/c (see Sec. 5.1.4) are also included in Fig. 14; the Xe+La points are very close to Pb+Pb/Au+Au results at the similar energies.

The results on the energy dependence of the K^+/π^+ ratio (*horn* plot) from the 10% most central Ar+Sc collisions are shown in Fig. 15 together with measurements in inelastic $p+p$, central Be+Be, central Pb+Pb and central Au+Au collisions. A clear distinction between the two data subsets is visible – $p+p$ and Be+Be results show similar values and collision energy dependence, while the heavy systems of Pb+Pb, Au+Au, and Ar+Sc show much higher K^+/π^+ ratios. Moreover, although Ar+Sc is clearly separated from small systems, its energy dependence does not show the horn seen in Pb+Pb and Au+Au reactions, exhibiting (within total uncertainties) a monotonic growth with collision energy both at mid-rapidity and for mean multiplicities. The most recent measurements for Xe+La collisions at 150A GeV/c (see Sec. 5.1.4) are also included in Fig. 15; the Xe+La points are close to Pb+Pb/Au+Au results at the similar energies.

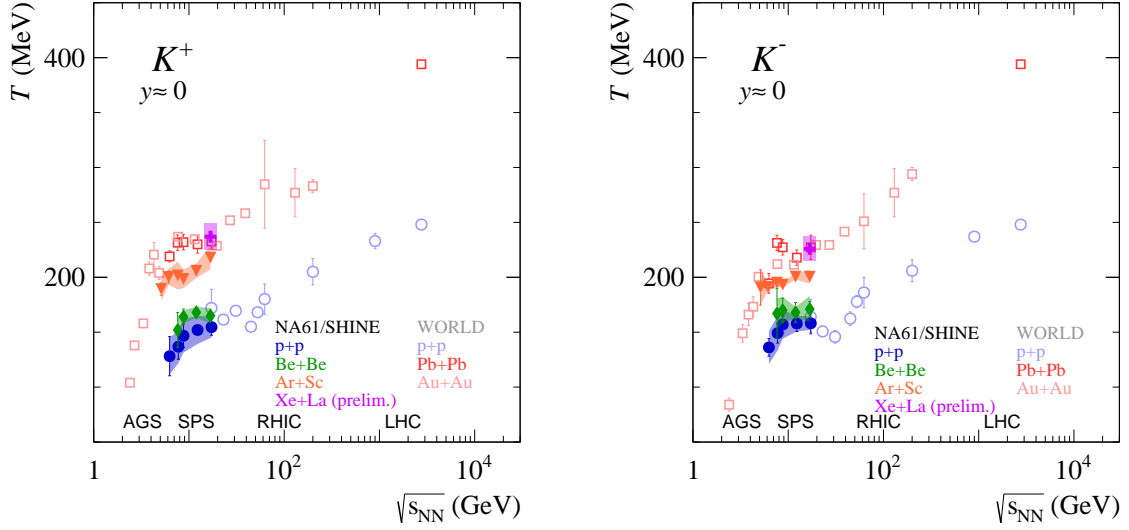


Figure 14: The energy dependence of the inverse slope parameter T of p_T spectra at mid-rapidity of positively (*left*) and negatively (*right*) charged K mesons for central Xe+La, Ar+Sc, Be+Be, Pb+Pb, and Au+Au collisions as well as inelastic $p+p$ interactions. Both statistical (vertical bars) and systematic (shaded bands) uncertainties are shown.

5.1.4. (OD, OF) Preliminary results on π^- , K^+ , and K^- production in 0–20% central Xe+La collisions at 150A GeV/c

The new results on π^- , K^+ , and K^- production in 0–20% central Xe+La collisions at 150A GeV/c have been just released as preliminary and shown at the Quark Matter Conference [23, 24]. The π^- spectra were obtained from the h^- method [25], where negatively charged pions are computed from negatively charged hadrons and the remaining contribution from other particles is corrected for using Monte Carlo data. The spectra of K^+ and K^- were obtained from dE/dx fits. The two-dimensional distributions of double-differential yields $d^2n/dydp_T$ of π^- , K^+ and K^- are presented in Fig. 16. From these plots the inverse slope parameters of kaon p_T spectra, as well as mid-rapidity yields and total multiplicities, are extracted and added to Figs. 14, 15, 17, 18, 19. The T parameters and mid-rapidity yields in *step* and *horn* plots are presented for the rapidity range $0.4 < y < 0.6$. For Xe+La results, only statistical uncertainties were estimated, whereas the systematic ones were assumed to be at the level of 5%.

5.1.5. Onset of fireball

The observed rapid change of hadron production properties that starts when moving from Be+Be to Ar+Sc collisions hints at some non-trivial threshold mechanism. Such system size dependence may be attributed to the beginning of the creation of large clusters of strongly interacting matter – *the onset of (QGP) fireball* [26]. The similarities of $p+p$ and Be+Be systems suggest that interactions of these systems could form small non-equilibrium clusters via binary collisions of nucleons, as in the Wounded Nucleon Model [27]. On the other hand,

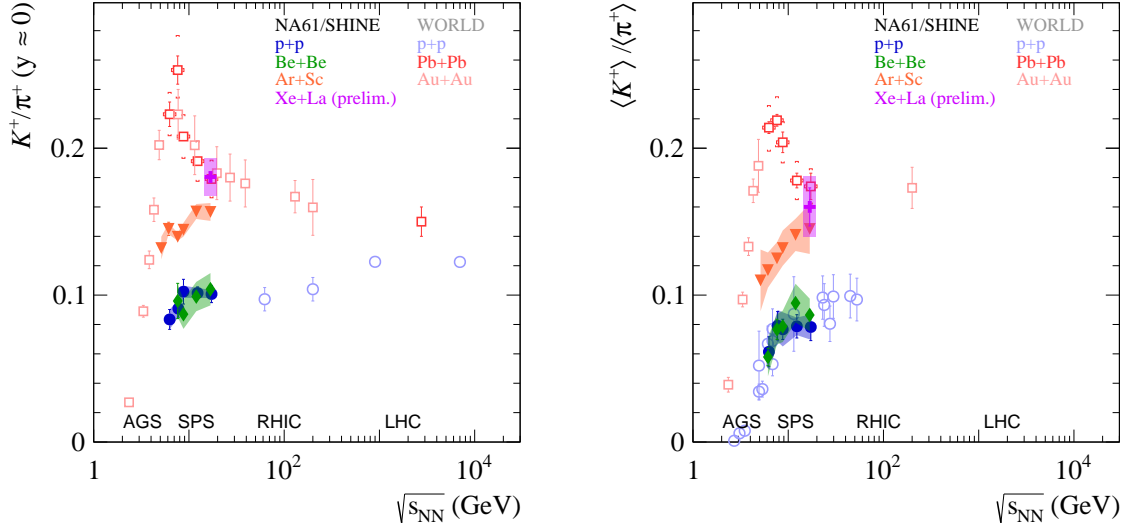


Figure 15: The energy dependence of the K^+/π^+ ratio at mid-rapidity (*left*) and for mean multiplicities (*right*) for central Xe+La, Ar+Sc, Be+Be, Pb+Pb, and Au+Au collisions as well as inelastic $p+p$ interactions. Both statistical (vertical bars) and systematic (shaded bands) uncertainties are shown.

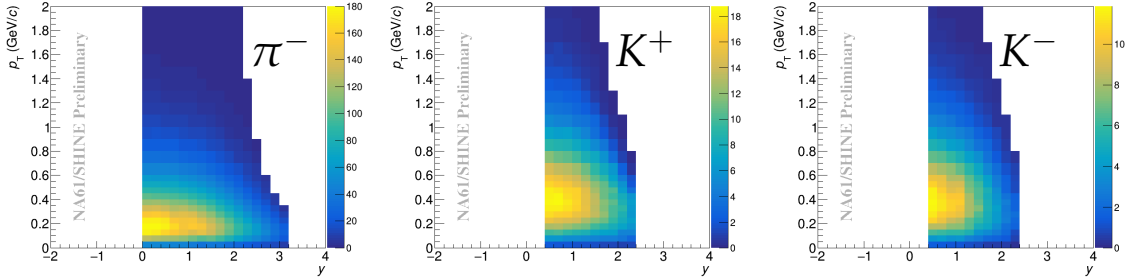


Figure 16: Two-dimensional distributions of double-differential yields $d^2n/dydp_T$ of π^- , K^+ and K^- produced in 0–20% central Xe+La interactions at 150A GeV/c.

properties of Pb+Pb collisions are well described by statistical and hydrodynamical models, which assume the creation of a collectively evolving fireball in (at least local) thermal equilibrium. Results on Ar+Sc collisions are clearly closer to the Pb+Pb ones than to $p+p$ and Be+Be measurements, hence *the onset of (QGP) fireball* may be identified at the system size close to the measured Ar+Sc reaction and may depend on collision energy. Such characteristic system size dependence is seen at multiple measured quantities: mean multiplicities ratios of $\langle K^+ \rangle / \langle \pi^+ \rangle$ (Fig. 17), the ratio of yields at mid-rapidity measurements K^+/π^+ (Fig. 18), inverse slope parameter T of K^+ transverse momentum spectra (Fig. 19). Recent phenomenological interpretations [28] suggest that the diagram of the high-energy nuclear collisions may, in fact, consist of three main domains in which certain hadron production processes dominate: i) creation, evolution, and decay of resonances, ii) formation, evolution and fragmentation of strings, and iii) creation, evolution and hadronization of QGP. Within this picture, the differences observed between the small systems ($p+p$, Be+Be) and Ar+Sc are an interplay of changeovers between these domains.

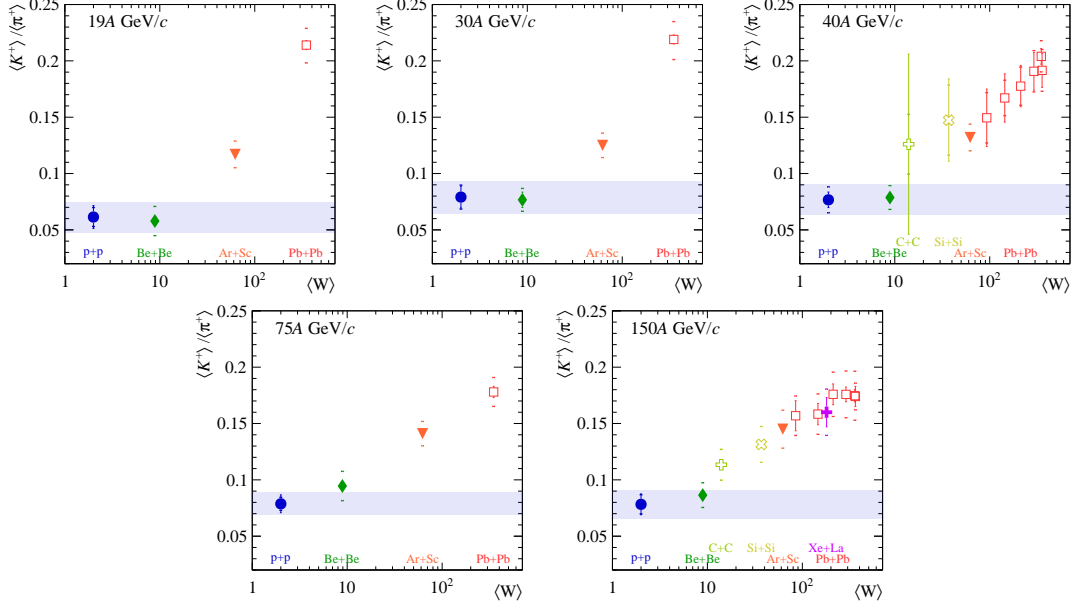


Figure 17: System size dependence of $\langle K^+ \rangle / \langle \pi^+ \rangle$ mean multiplicity ratios measured at 19(20)A–150(158)A GeV/c, showing values for inelastic $p+p$ interactions and central Be+Be, Ar+Sc, Xe+La, and Pb+Pb. The system size is represented by the mean number of wounded nucleons ($\langle W \rangle$). Statistical uncertainties are shown as bars and systematic ones are denoted with square braces. The shaded band shows the total uncertainty of the $p+p$ result.

5.1.6. (O, OD) Preliminary results on K_S^0 production in inelastic $p+p$ collisions at 31 and 40 GeV/c

The yields of K_S^0 mesons produced in inelastic $p+p$ interactions at beam momenta of 31 and 40 GeV/c were measured with the NA61/SHINE spectrometer [29]. Measurements of double-differential spectra and mean multiplicities of K_S^0 mesons were performed. The K_S^0 yields in different rapidity bins were obtained from the corresponding measured transverse momentum distributions. Extrapolation to the high p_T region outside of the acceptance was performed using the function $f(p_T) = A \cdot p_T \cdot \exp(-\sqrt{p_T^2 + m_0^2}/T)$, where m_0 is the mass of the K_S^0 [30] and T is the inverse slope parameter.

The mean multiplicities of K_S^0 mesons were calculated as the sum of the measured data points and the integrals in the unmeasured regions obtained from a linear fit to the two data points at $y \geq 1$. The obtained mean multiplicities are summarized in Table 1 and compared in Fig. 20 with the results from other experiments in the energy range from 3 to 32 GeV. The measured values are seen to rise linearly with collision energy $\sqrt{s_{NN}}$; the NA61/SHINE results follow the observed trend.

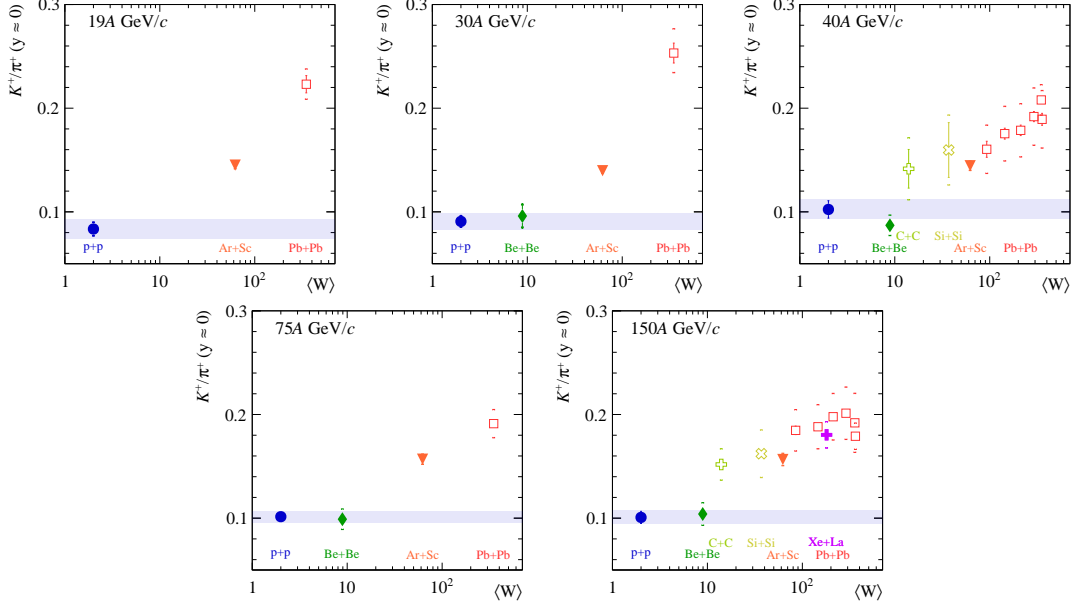


Figure 18: System size dependence of K^+/π^+ ratios at mid-rapidity measured at 19(20)A–150(158)A GeV/c, showing values for inelastic $p+p$ interactions and central Be+Be, Ar+Sc, Xe+La, and Pb+Pb. The system size is represented by the mean number of wounded nucleons ($\langle W \rangle$). Statistical uncertainties are shown as bars and systematic ones are denoted with square braces. The shaded band shows the total uncertainty of the $p+p$ result.

p_{beam} (GeV/c)	Mean multiplicity	Statistical uncertainty	Systematic uncertainty
31	6.1×10^{-2}	0.2×10^{-2}	0.5×10^{-2}
40	8.0×10^{-2}	0.1×10^{-2}	0.4×10^{-2}
80	12.0×10^{-2}	0.1×10^{-2}	0.5×10^{-2}
158	16.2×10^{-2}	0.1×10^{-2}	1.1×10^{-2}

Table 1: The mean multiplicities of K_S^0 mesons measured by NA61/SHINE in inelastic $p+p$ interactions with beam momenta $p_{\text{beam}} = 31, 40, 80,$ and 158 GeV/c.

5.1.7. (O, OD) Preliminary results on K_S^0 production in 0–10% central Ar+Sc collisions at 75A GeV/c

The preliminary results on K_S^0 production in 0–10% central Ar+Sc collisions at 75A GeV/c were measured by NA61/SHINE. The results were presented at several conferences, including Quark Matter 2023 [33]. The mean multiplicity of produced K_S^0 mesons was calculated as the integral of the fitted rapidity function and equals $\langle K_S^0 \rangle = 6.25 \pm 0.09$ (stat) ± 0.73 (sys).

An unexpected excess of production of charged ($K^+ + K^-$) over neutral (K_S^0) mesons was reported. Strong interactions preserve approximately isospin (I) and its third component (I_z), which, among others, for collisions of $N = Z$ nuclei (N – number of neutrons, Z – number of protons) corresponds to equivalence in the production of new pairs of $u - \bar{u}$ and $d - \bar{d}$ quarks [34]. Following Smushkevich rule, for all particles involved in isospin-conserving reactions, all members of isospin multiplets are produced in equal numbers if and only if the initial population is uniform [35–37]. Thus, for an electric-to-baryon charge

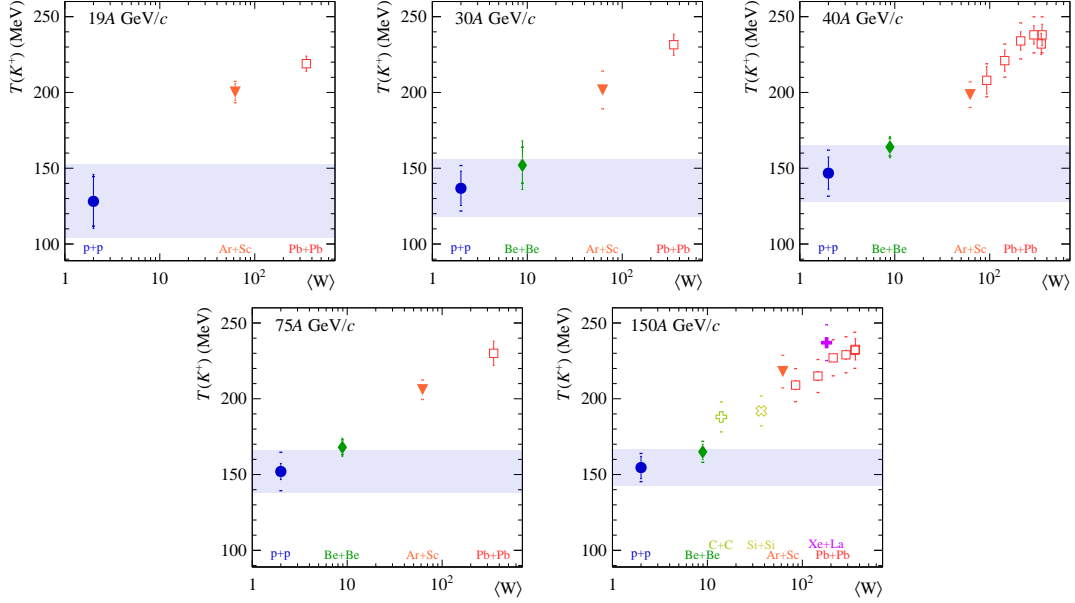


Figure 19: System size dependence of the inverse slope parameter T of K^+ transverse momentum spectra at mid-rapidity measured at 19(20)A–150(158)A GeV/c, showing values for inelastic $p+p$ interactions and central Be+Be, Ar+Sc, Xe+La, and Pb+Pb. The system size is represented by the mean number of wounded nucleons ($\langle W \rangle$). Statistical uncertainties are shown as bars and systematic ones are denoted with square braces. The shaded band shows the total uncertainty of the $p+p$ result.

ratio (Q/B ; $Q \equiv Z$) equal to $1/2$ ($I = I_z = 0$) and in the case of exact isospin symmetry we expect the following relations between kaon multiplicities: $K^+(u\bar{s}) = K^0(d\bar{s})$ and $K^-(\bar{u}s) = \bar{K}^0(\bar{d}s)$. By summing up the equations one obtains: $K^+ + K^- = K^0 + \bar{K}^0$. The K^0 and \bar{K}^0 mesons are not directly measured in detectors since the physical neutral states are the K_S^0 and K_L^0 . Neglecting a very small effect of the CP violation, the production of K_S^0 should be given by: $K_S^0 = \frac{K^0 + \bar{K}^0}{2}$. Therefore, we expected the relation between multiplicities: $K_S^0 = \frac{K^+ + K^-}{2}$.

The left panel of Fig. 21 shows the comparison of rapidity spectrum of neutral (K_S^0) with the average spectrum of charged (K^+ and K^-) mesons [22] ($K^{+/-} = \frac{K^+ + K^-}{2}$). A similar plot but for transverse momentum spectra is presented in the right panel of Fig. 21. Additionally, for transverse momentum spectra, the R_k ratio is plotted, where $R_k = \frac{K^{+/-}}{K_S^0}$. A significant difference between $K^{+/-}$ and K_S^0 yields is observed for both rapidity and transverse momentum spectra.

Figure 22 presents the compilation of available data on the ratio of charged to neutral kaons as a function of collision energy. The systematic excess of the production of charged kaons is visible in the presented nucleus-nucleus data. The world data, having large uncertainties of individual points, support the NA61/SHINE finding.

The comparison of the charged-to-neutral kaon ratio to the predictions of the Hadron Resonance Gas (HRG) model [38] is presented in Fig. 23 (taken from Ref. [39]). The black line shows the HRG baseline for electric-to-baryon charge $Q/B = 0.4$. For Ar+Sc collisions Q/B

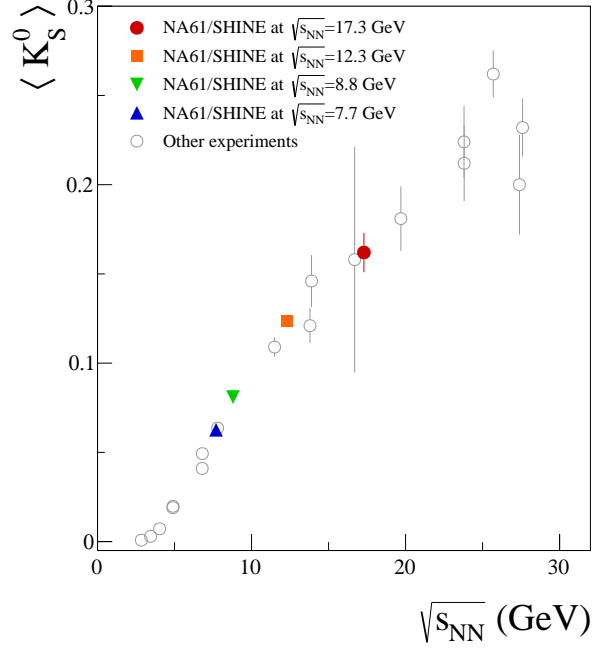


Figure 20: Collision energy dependence of mean multiplicity of K_S^0 mesons produced in $p+p$ interactions. The results from NA61/SHINE are presented with colored symbols: the full colored red circle shows the measurement at beam momentum $p_{\text{beam}} = 158$ GeV/c [31], the full colored orange square indicates the measurement at beam momentum $p_{\text{beam}} = 80$ GeV/c [32], the full colored green triangle down represents the measurement at beam momentum $p_{\text{beam}} = 40$ GeV/c [29] and the full colored blue triangle up corresponds the measurement at beam momentum $p_{\text{beam}} = 31$ GeV/c [29]. All the results from the NA61/SHINE are presented with their total uncertainties. The results published by other experiments are presented with open circles colored in gray.

= 0.45 (Ar) and $Q/B \approx 0.47$ (Sc), whereas $Q/B \approx 0.4$ corresponds to Pb or Au nuclei. The black dots in Fig. 23 represent the HRG baseline for Q/B values specified according to the given types of colliding nuclei. The prediction of HRG takes into account a set of known effects that violate isospin symmetry, or preserve it but still can lead to a deviation of R_k from unity [36]. Nevertheless, the predicted deviation from the expected value of $R_k = 1$ is significantly smaller than for the experimental data. Thus, the presented result is to be considered as evidence for effects that go beyond the ones predicted by the HRG model. It is at present a subject of active scrutiny whether this result could be an indication of the violation of isospin symmetry being significantly stronger than commonly assumed for high-energy nuclear collisions.

5.1.8. (O, OD) Preliminary results on Λ production in 0–10% central Ar+Sc collisions at 75A GeV/c

The preliminary measurements of the double-differential spectra and mean multiplicity of Λ baryons produced in 0–10% central Ar+Sc collisions at 75A GeV/c were conducted [40]. One-

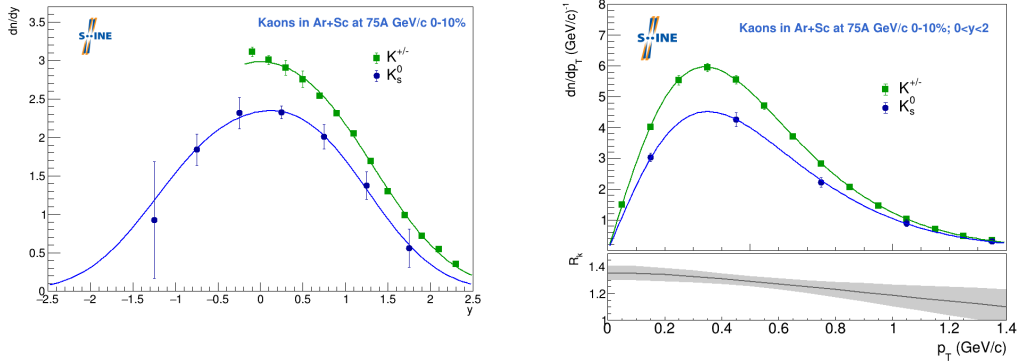


Figure 21: *Left:* Comparison of rapidity spectrum of neutral (K_S^0) with the average spectrum of charged (K^+ and K^-) mesons in 0–10% central Ar+Sc collisions at 75A GeV/c. The total uncertainties are plotted and calculated as the square root of the sum of squared statistical and systematic uncertainties ($\sqrt{\text{stat}^2 + \text{sys}^2}$). For charged kaons [22], the total uncertainties were calculated separately for positively charged and negatively charged kaons and then propagated. *Right:* same as *left* but for transverse momentum spectra.

dimensional transverse momentum spectra are fitted with an exponential function in order to obtain the inverse slope parameter T and extrapolate spectra to the unmeasured high p_T region. The obtained one-dimensional rapidity spectrum is shown in Fig. 24 together with the prediction of the EPOS1.99 [20, 21] model, which underestimates the Λ yields by 20–25%.

The mean multiplicity $\langle \Lambda \rangle$ is calculated from the sum of measured data points scaled under the assumption that the ratio between measured and unmeasured regions is the same in data and Monte Carlo simulation. The obtained mean multiplicity of Λ baryons equals 6.44 ± 0.24 (stat) ± 1.10 (sys). The $\langle \Lambda \rangle / \langle \pi^+ \rangle$ ratio is then compared for different collision systems as shown in Fig. 25. One can see that it follows a similar trend to that of $\langle K^+ \rangle / \langle \pi^+ \rangle$ ratio.

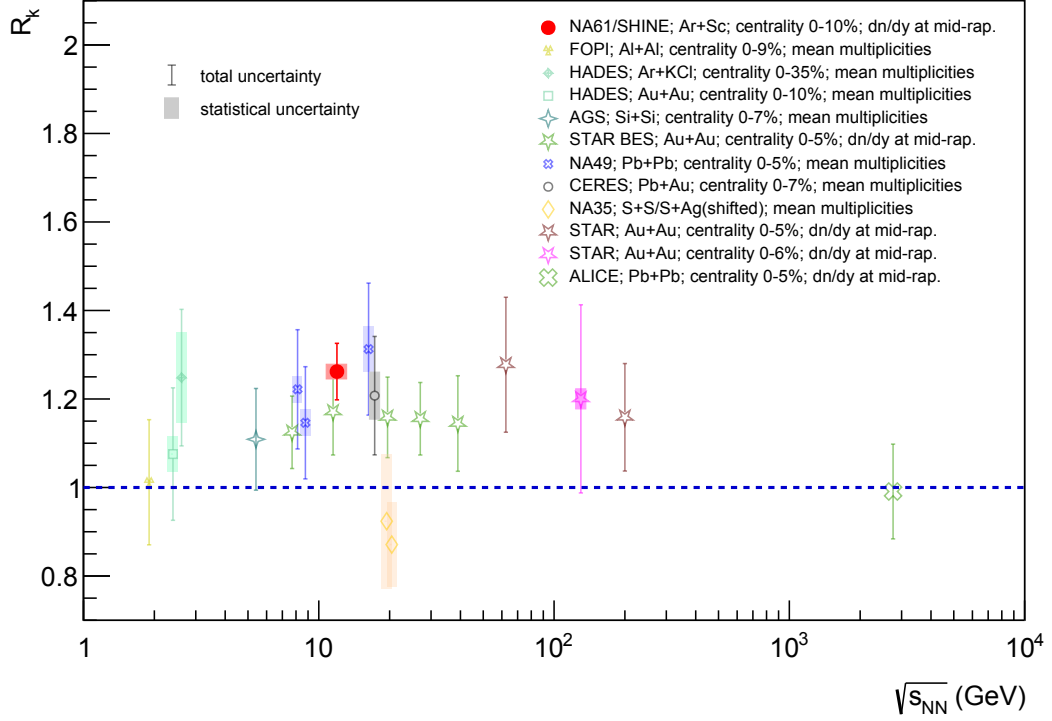


Figure 22: Compilation of the available data on the ratio of charged to neutral kaons as a function of collision energy. The measurement from NA61/SHINE is shown as a red dot. See Ref. [33] for a complete list of references to the world data needed to obtain R_k values.

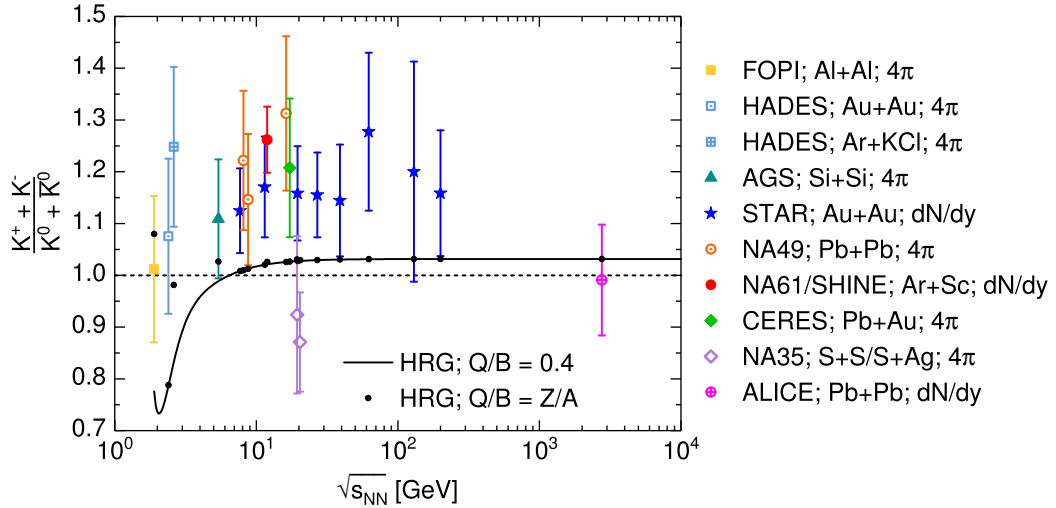


Figure 23: Comparison of charged-to-neutral kaon ratio ($K^0 + \bar{K}^0$; in HRG equal $2K_S^0$) with predictions of the Hadron Resonance Gas model [38]. The black line shows the HRG baseline for electric-to-baryon charge ratio $Q/B = 0.4$. Black dots represent the HRG baseline for Q/B values specified according to the given types of colliding nuclei. Figure taken from Ref. [39].

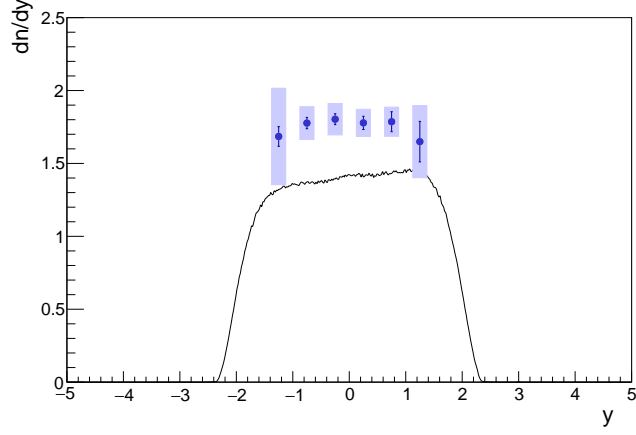


Figure 24: Rapidity spectrum of Λ baryons produced in 0–10% central Ar+Sc collisions at 75A GeV/c, compared with EPOS1.99 [20,21].

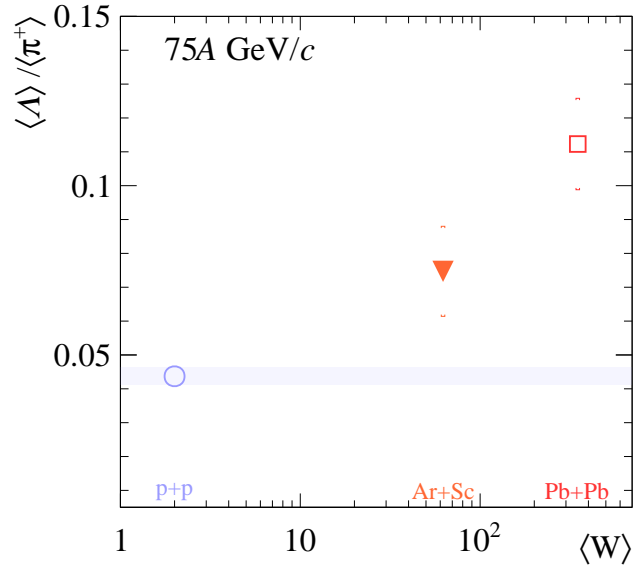


Figure 25: The system size dependence of $\langle \Lambda \rangle / \langle \pi^+ \rangle$ ratio in full 4π phase space. Statistical uncertainties are shown as bars, and systematic ones are denoted with square braces. The shaded band shows the total uncertainty of the $p+p$ result. The numerical data needed to obtain $p+p$ and Pb+Pb points at similar energies were taken from Refs. [41,42] (Λ baryons in $p+p$ and Pb+Pb) and Refs. [43,44] (pions in $p+p$ and Pb+Pb).

5.2. New results for neutrino and cosmic-ray physics

For many years, the NA61/SHINE Collaboration has had a program of hadron production measurements for long-baseline neutrino oscillation experiments at J-PARC and Fermilab (FNAL). These measurements improve knowledge of the neutrino flux produced in accelerator-based neutrino beams. NA61/SHINE measures total cross-sections and differential spectra of hadron yields from thin and replica neutrino beam targets.

NA61/SHINE also performs hadron production measurements relevant to interpreting extensive air shower data (EAS) at ultra-high energies and measures production and fragmentation cross-sections to understand Galactic cosmic-ray data (GCR).

5.2.1. Neutral hadrons from $p+C$ at 120 GeV/c interactions (FNAL)

The interaction of 120 GeV/c protons with carbon is of particular interest to the neutrino community because it represents the primary interaction that creates the NuMI neutrino beam [45] at Fermilab, which serves the MINERvA [46] and NOvA [47] neutrino physics experiments. This reaction, along with those on replica neutrino production targets, was the motivation for the development of the Forward TPC (FTPC) system [48].

NA61/SHINE has published two papers, one on the production of charged hadrons and one on the production of neutral hadrons in 120 GeV/c $p+C$ interactions. Both were based on data collected in the 2016 and 2017 run periods when the spectrometer operated with different magnetic fields and detector configurations (the FTPCs were added in 2017). The results are now available for use in interaction and flux simulators and are being incorporated into Fermilab's PPFX neutrino flux prediction package [49].

The neutral hadron analysis was submitted in 2022 and published in 2023 [50]. Results included production yields of K_S^0 , Λ , and $\bar{\Lambda}$, identified using an invariant mass and momentum asymmetry selection from reconstructed two-particle secondary vertices. The results are binned in production angle and particle momentum, making these the first fully double-differential yield measurements for this process at this energy. Yields for a single angular bin are shown in Fig. 26.

5.2.2. Charged hadrons from $p+C$ at 120 GeV/c interactions (FNAL)

NA61/SHINE has also made measurements of charged hadron production from 120 GeV/c $p+C$ interactions. These results [51], also from the 2016 and 2017 data sets, have been just published in *Phys. Rev. D*. They will also be used in the near future to improve flux estimations for Fermilab neutrino experiments. The measurement of forward proton production, which is essential for estimating secondary interactions in long targets, benefits significantly from the addition of the FTPCs (Fig. 27).

Measured multiplicities of charged pions in two selected angular bins are shown in Fig. 28. Predictions from several Monte Carlo generators are shown for comparison. In most hadron

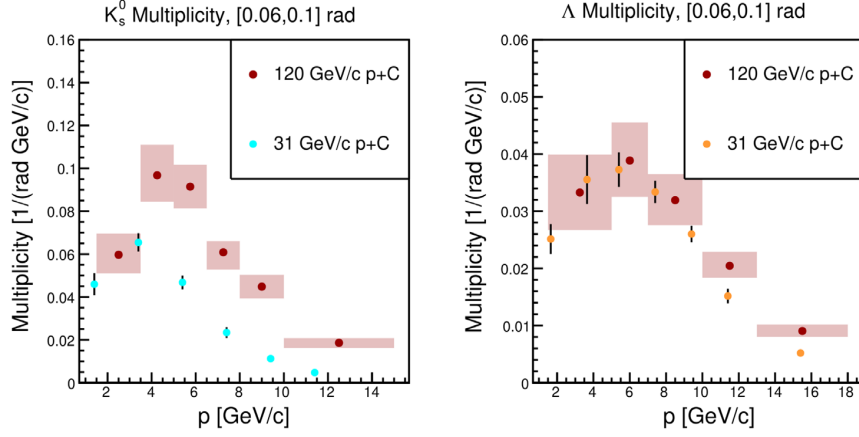


Figure 26: Spectrum of K_S^0 and Λ in a selected angular bin from 120 GeV/c $p+C$ interactions. Similar production rates from NA61/SHINE at 31 GeV/c are shown for comparison.

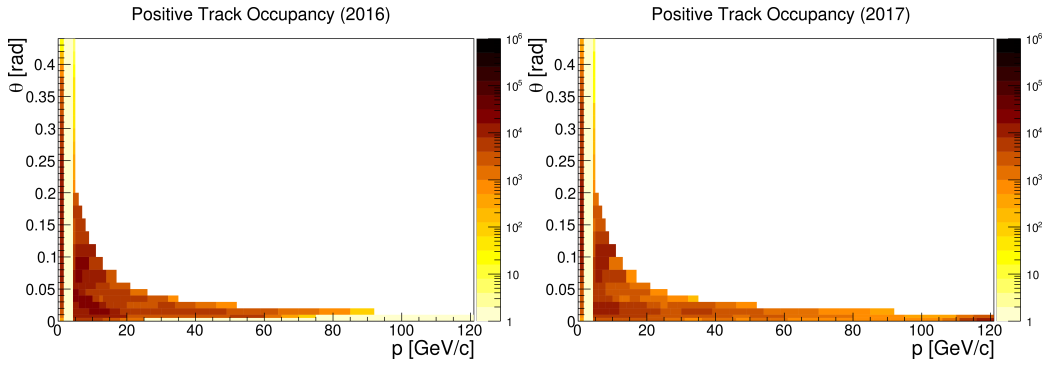


Figure 27: Track occupancy comparison for proton candidate tracks between 2016 data set (*left*) and 2017 (*right*). Note the significantly increased occupancy in the forward, high-momentum region for the 2017 analysis which includes data from the FTPCs. The empty region at low momentum corresponds to the omitted Bethe-Bloch crossing region for protons and pions, where particle identification performance is poor.

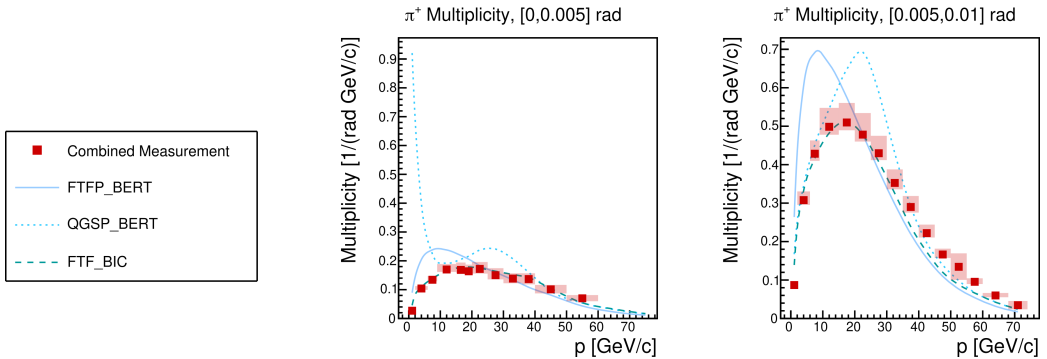


Figure 28: Spectra of π^+ production in 120 GeV/c $p+C$ interactions in two selected angular bins. Monte Carlo simulations using different interaction generators are shown.

interactions important for neutrino physics, Monte Carlo generators have major disagreements over large regions of phase space and no single model predicts the data observations except in limited ranges.

5.2.3. Neutrino analyses in progress

p+C at 90 GeV/c (FNAL): The analysis of the 2017 *p+C* at 90 GeV/*c* data is currently being performed, with plans for measurements of neutral and charged hadron production. The data set is fully calibrated, and the neutral hadron production will be measured first and then used as an input for the charged hadron analysis. In the 2017 data set, a trigger issue prevented the reaction's total cross-section measurement. To measure the total cross-section, a new *p+C* at 90 GeV/*c* data set was taken in July 2023; this data set will be analyzed to extract the reaction's cross-section.

p+C at 60 GeV/c (FNAL): The differential yields of neutral particles (K_S^0 , Λ , $\bar{\Lambda}$) and charged particles (π^\pm , K^\pm , p , \bar{p}) from the 60 GeV/*c* protons on carbon interactions were previously measured and reported in Sec. 2.2.2 of Ref. [52]. However, the neutral particle results showed discrepancy compared to proton-carbon interactions at different momenta. The neutral and charged analyses of this data set have been re-started using native SHINE reconstruction to address the above problem.

p+NOvA target at 120 GeV/c (FNAL): The 2018 NOvA replica target geometry has been implemented into the SHINE framework. A Monte Carlo simulation data set has been generated to confirm the simulated target geometry and position. An updated particle vertexing algorithm was also introduced to SHINE. This algorithm was created to extrapolate particle tracks back to the surface of the long target. Following this, the 2018 NOvA target replica data set has undergone various calibration steps. First, the distance between the beam position detectors and the NA61/SHINE TPCs was calibrated. Measuring this distance allows for calibrating the relative positions of the rest of the TPCs and accurately reconstructing where protons interacted inside the NOvA target. Next, target alignment was determined for the 2018 summer data. Any target position shifts and tilts were recorded for use in the NA61/SHINE simulation of the replica target. Finally, the global track residuals were calculated for each binned TPC to account for any systematic shifts in the reconstruction (small chamber position shifts, electrostatic effects, etc.).

The analysis procedure is being developed concurrently with calibration. The 2016 proton-proton analysis procedure has been adapted to process Monte Carlo samples from the 2018 data in preparation for charged and neutral hadron production rate measurements. Reusing the same analysis procedure for the 2016, 2018, and future DUNE replica target results will reduce the time to produce publications and enable consistency between related results.

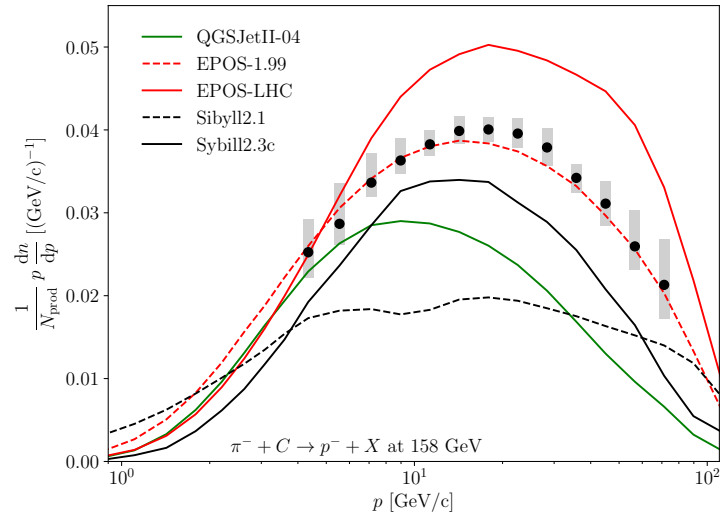
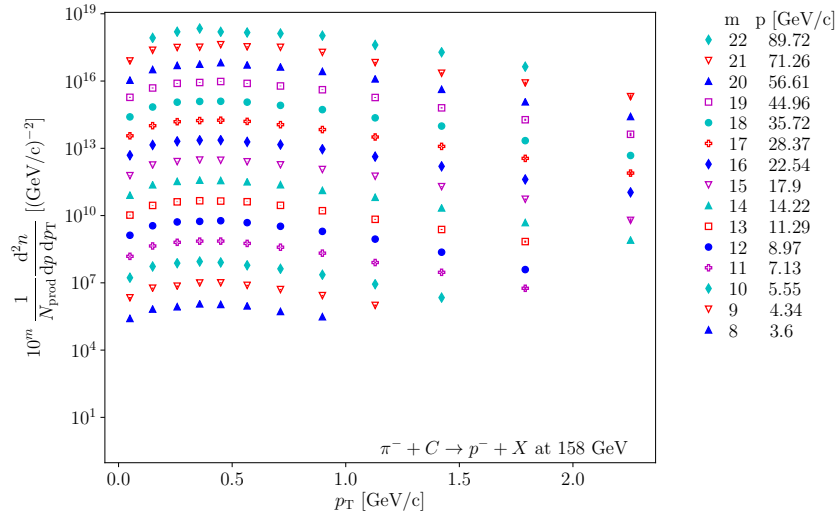


Figure 29: NA61/SHINE results on anti-proton production in $\pi^- + C$ interactions at 158 GeV/c [53]. The p_T spectra at different particle momenta p are displayed on the top (error bars are smaller than the markers) and the p_T -integrated spectra are shown on the bottom and compared to predictions of hadronic interaction models [21, 54–57].

p +T2K target at 31 GeV/c (J-PARC): The calibration of the 2022 p +T2K at 31 GeV/c data started with the reconstruction and the calibration of the BPD data. The GEM BPD detectors were aligned with respect to the two Delay Wire Chambers (DWC) used during the BPD calibration run. Also, some calibrations related to the TDC of the S1 scintillator detector are ongoing. One is the calculation of the mean time offset of the timing of S1 and L2 triggers to clear the S1 hit corresponding to the L2 trigger, and the other is the calculation of the time phase shift between S1 and the start of the TPC time sampling. These results will be used for the TPC drift velocity calibration in the next step.

5.2.4. Final results on $\pi^- + \text{C}$ at 158 and 350 GeV/c (EAS)

Within the reporting period, we published the measurement of the p - p_T spectra of π^\pm , K^\pm , p , \bar{p} , Λ , $\bar{\Lambda}$, and K_S^0 produced in interactions of negatively charged pions with carbon nuclei at beam momenta of 158 and 350 GeV/c [53]. Together with the previous publication of the production spectra of ρ^0 , ω and K^{*0} mesons in $\pi^- + \text{C}$ interactions [58], we therefore successfully completed our hadron production studies for the understanding of air showers induced by ultra-high energy cosmic rays. The spectra measured with NA61/SHINE provide a unique reference data set with unprecedented precision and large phase-space coverage to tune models for particle production in extensive air showers where pions are the most numerous projectiles. As an example of the many reactions measured, the spectra of produced anti-protons are shown in Fig. 29. In the top panel, the p - p_T spectra are displayed, and the bottom panel shows the comparison of the p_T -integrated spectra to predictions of hadronic interaction models used to interpret air showers. Anti-proton production is particularly interesting for air shower physics, as it traces the overall baryon production driving the hadronic component of air showers [59]. As can be seen, the measurements of NA61/SHINE provide the necessary data to tune the hadronic interaction models. They thus are an essential input to solve the “muon puzzle” at ultra-high energies, see, e.g., Ref. [60].

5.2.5. Preliminary result on the production of boron isotopes (GCR)

Nuclear fragmentation cross-sections and the secondary-to-primary flux ratios are crucial parameters for modeling the propagation of cosmic rays in the Galaxy. Large cross-section uncertainties currently dominate the propagation characteristics. The precision of recent flux measurements by space detectors like AMS-02, CALET, and DAMPE [61–63] implores the need for measuring fragmentation cross-sections with a precision $< 5\%$. The B/C flux ratio is the simplest to measure and is the most well-studied secondary-to-primary ratio. Hence, a precise nuclear fragmentation cross-section leading to boron production will aid in studying transport parameters. In 2018, a pilot run demonstrated the feasibility of performing fragmentation studies with NA61/SHINE. We have derived the total boron production [64] and the ^{11}C production [65] in $^{12}\text{C} + p$ reaction at $13.5A$ GeV/c using the polyethylene (PE) and graphite (C) targets. Most recently, the production cross-sections of boron isotopes (^{11}B and ^{10}B) were measured and presented at the 38th International Cosmic Ray Conference [66].

A fit to the distribution of boron fragments in the MTPC for the three target settings, PE, C, and the empty target holder (OUT), is shown in Fig. 30. The preliminary results are shown in Fig. 31. As can be seen, they agree well with previous measurements. Given that these results are from a three-day pilot run with the old data acquisition system, their uncertainties are currently dominated by statistical uncertainties. A future dedicated high-statistics run for studying the fragmentation of various primary C, N, O, and Si nuclei into lighter fragments will improve the precision of this measurement to the desired precision needed to study the propagation and escape of cosmic rays in our Galaxy, as detailed in Appendix A.

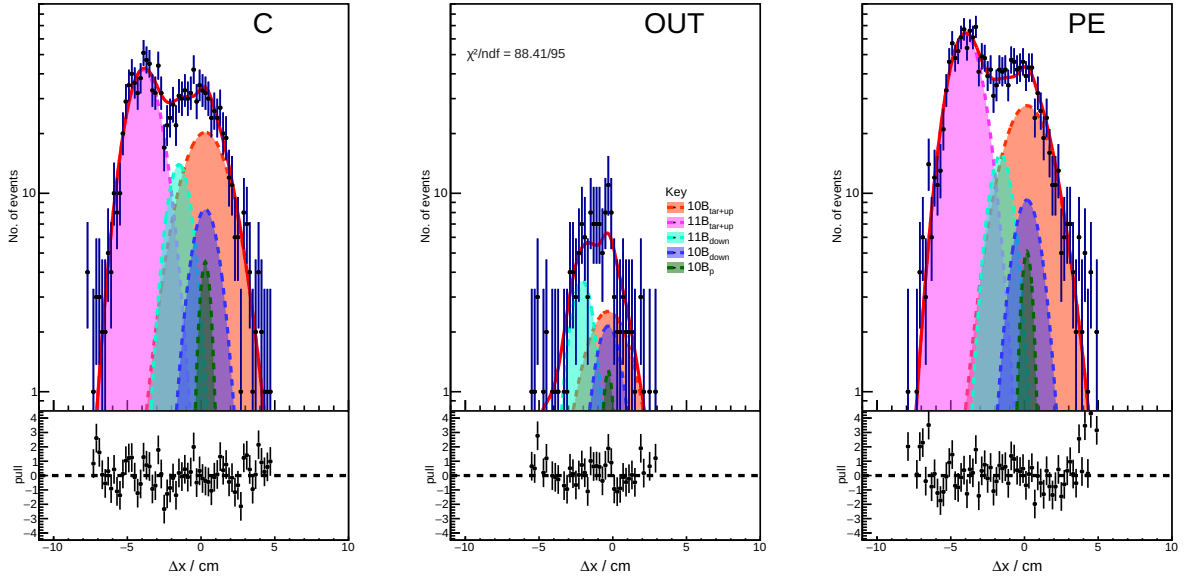


Figure 30: Fit results of the boron isotope fragments in the MTPC for the three target settings, C, OUT, and PE. The x -axis, Δx depicts the deflection of the fragments in the magnetic field relative to the $A/Z = 2$ particles at $\Delta x = 0.0$ cm. Boron fragments produced outside and downstream of the target (green and blue peaks) are also fitted; hence, they do not interfere with the signal from the fragments produced inside the target (orange and pink peaks).

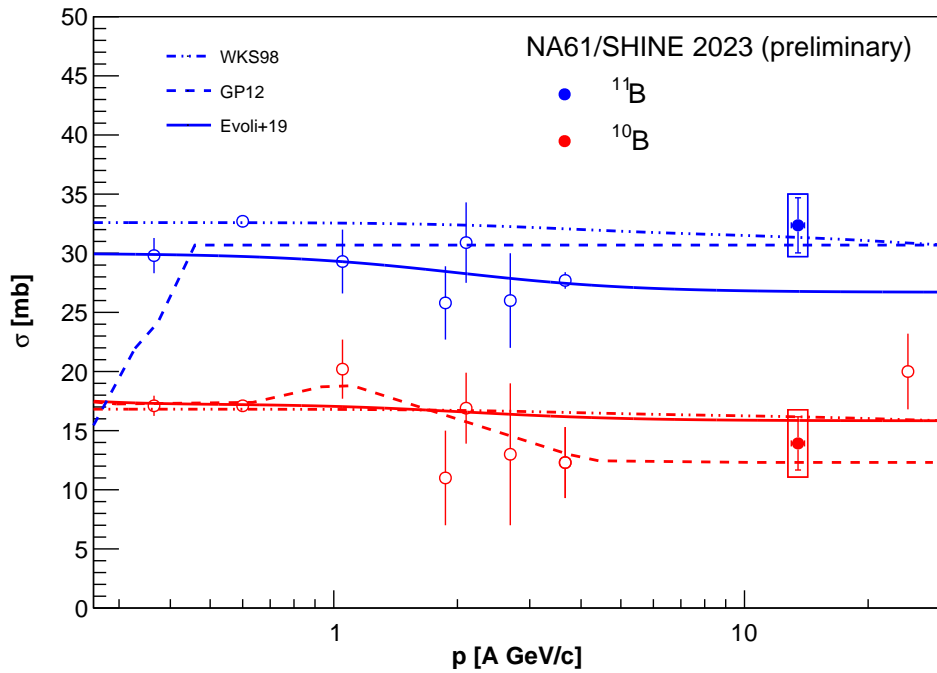


Figure 31: Preliminary result on the production of the two boron isotopes in $^{12}\text{C}+p$ reaction. Previous measurements are shown as open symbols, and the lines represent different parametrizations of the cross-sections with respect to the momentum per nucleon [67–71]. The vertical line represents the statistical uncertainty of our measurement, whereas the box represents the total uncertainty, including systematics.

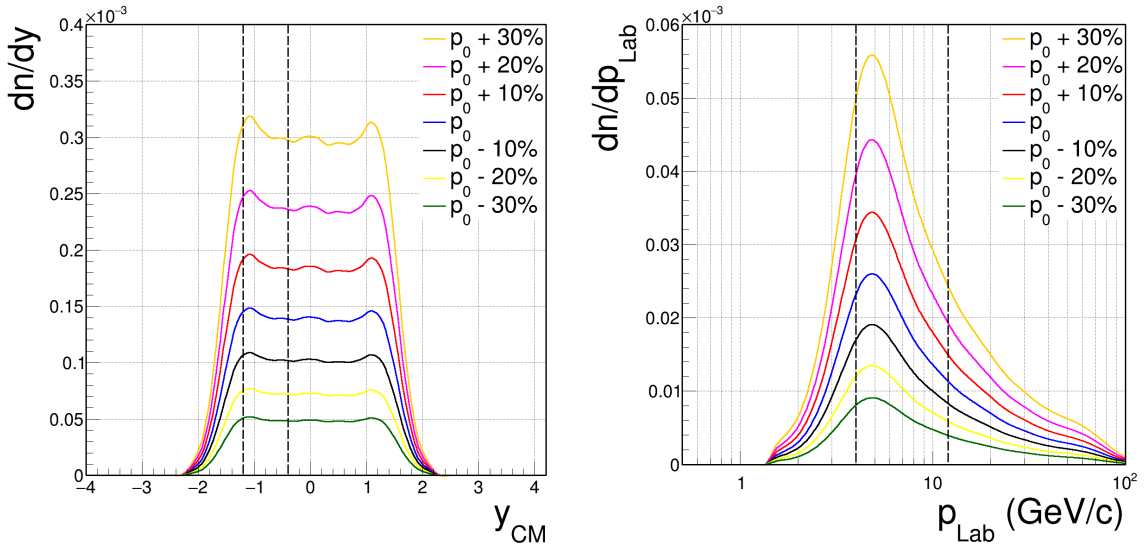


Figure 32: Simulated deuteron spectra for rapidity in the center-of-mass frame (denoted y_{CM}) (left) and momentum in the laboratory frame (denoted p_{Lab}) (right). The $p+p$ interactions were simulated at $p_{\text{beam}} = 158$ GeV/c, and the conditions from the coalescence model were applied to produce deuteron spectra for seven different values of the coalescence momentum p_0 . This was done to evaluate the kinematic phase space, which is accessible to the $\text{tof} - dE/dx$ analysis in NA61/SHINE and is shown here between the vertical dashed lines.

5.2.6. Towards deuteron production cross-section measurements in $p+p$ collisions at 158 GeV/c (GCR)

Detecting cosmic anti-nuclei can be a breakthrough approach for identifying dark matter [72]. The primary source of cosmic anti-nuclei background are interactions between cosmic-ray protons and interstellar hydrogen gas. Gaining a deeper insight into deuteron production in $p+p$ interactions is an essential first step in modeling these astrophysical processes [73, 74]. The two most prevalent formation models, the thermal and coalescence models, are based on different underlying physics. A better understanding of (anti)nuclei production mechanisms is needed, which drives the effort to analyze high-statistics data sets from fixed-target experiments [75].

This deuteron analysis is based on the 158 GeV/c $p+p$ data sets collected in 2009, 2010, and 2011 with a total of about 65 M events. Deuteron production is rare in $p+p$ interactions at SPS energies of $\sim 100\text{--}400$ GeV. For $p_{\text{beam}} = 158$ GeV/c, the coalescence parametrization developed in Refs. [73, 74] predicted a per-event production probability of 0.0004, with an uncertainty band from 0.0002–0.0009. Using these estimates, about $\sim 10,000\text{--}60,000$ deuterons should have been produced in the high-statistics $p+p$ data. However, because of the limited phase space acceptance of the detector, only a fraction of the total deuterons produced can be identified.

Deuteron identification in data relies on mass reconstruction and requires ToF information in addition to the dE/dx information. The ToF calibration was recently completed. To evaluate the kinematic phase space which is accessible to the $\text{tof} - dE/dx$ analysis, about 2.7 trillion

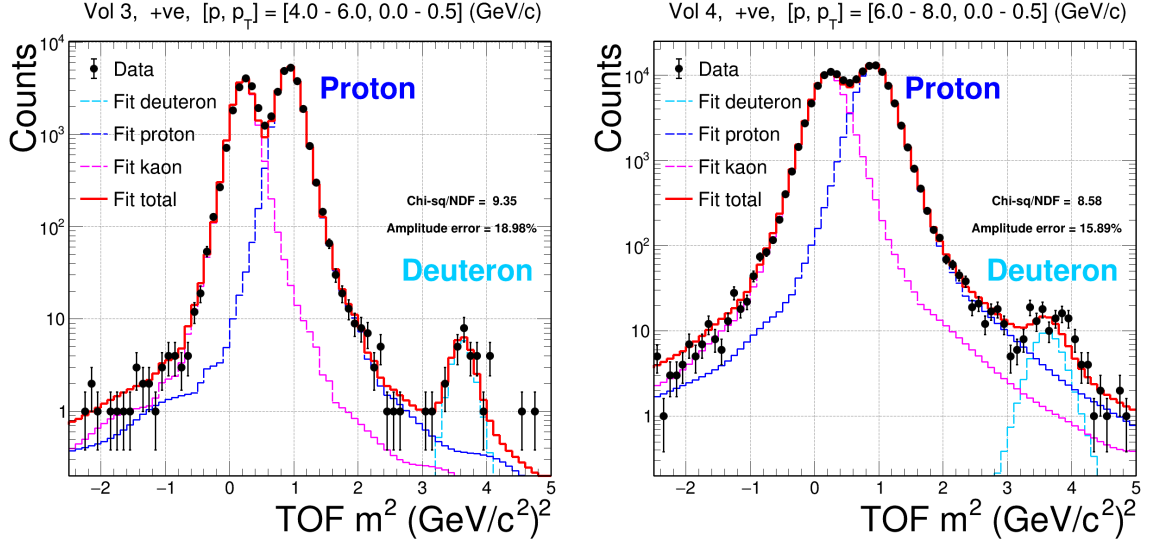


Figure 33: Data-driven pion mass template fits used to fit the kaon, proton, and deuteron peaks and tail regions, shown here for two example phase space bins. Data and fitted protons, kaons, and deuterons are shown. A clear deuteron signal is visible in both bins. A correct estimate of the proton tail under the deuteron signal is critical.

$p+p$ interactions were simulated at $p_{\text{beam}} = 158$ GeV/c using the EPOS-LHC model [56] and a coalescence model afterburner described in Refs. [73,74]. Figure 32 (left) presents the predicted deuteron rapidity spectra in the center-of-mass frame. The deuteron rapidity region accessible to the ToF detectors is represented within the vertical black lines and coincides with peak deuteron production in the center-of-mass frame's backward hemisphere. As the available energy in this collision system is limited ($\sim \sqrt{s} = 17.3$ GeV), most deuterons in these interactions are generated at low momentum. Figure 32 (right) shows the deuteron laboratory momentum spectra predicted by the coalescence model for different values of p_0 . The vertical black lines illustrate that most deuterons are expected to be produced within the momentum phase space accessible to the $\text{tof} - dE/dx$ analysis.

A data-driven template fitting method was developed for particle identification. For a given (p, p_T) bin, pions and positrons were separated from the other particles using the dE/dx information. As the mass distributions for kaons, protons, and deuterons overlap, the pion mass distribution was modified for detector resolution effects and the kaon, proton, and deuteron mass, respectively, to serve as the input for the combined template fit of the higher-mass $Z = 1$ -particle mass spectrum. Figure 33 shows an example for two (p, p_T) bins and reveals clear deuteron peaks and the importance of a realistic estimation of the proton tail in the deuteron mass region. The extraction of the deuteron yield is based on the probability or likelihood particle identification method, already developed for the dE/dx -only analysis.

Detailed cross-checks have been developed to account for the deuterons produced by secondary protons in the target material or holder. The contribution of secondary protons interactions with the right target holder was estimated to be negligible, and the liquid hydrogen target was estimated to be $\sim 5\%$ [75]. The correction factors for detector geometry were calculated using Monte Carlo simulations, and ToF-related efficiency calculations are ongoing.

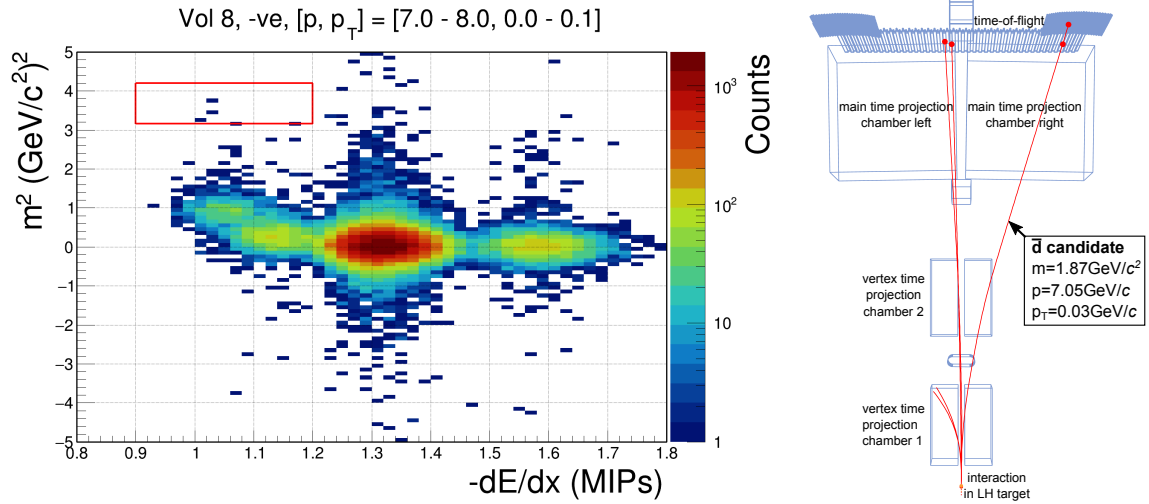


Figure 34: *Left:* Initial measurements of negative-charged particles with the distribution of m^2 versus dE/dx in a two-dimensional kinematic phase space bin, using the $tof - dE/dx$ analysis in $p+p$ 158 GeV/c in NA61/SHINE. Anti-protons, K^- , π^- , and electrons can be identified. The expected anti-deuteron region is also shown within the red box. *Right:* An anti-deuteron candidate in $p+p$ 158 GeV/c.

Systematic and statistical uncertainties will be estimated next. The preliminary release of these results will follow after that.

5.2.7. Cosmic-ray analyses in progress

Beryllium and lithium fragmentation (GCR): The beryllium isotopes ^{10}Be and ^9Be are secondary nuclei resulting from primary cosmic-ray fragmentation in the Galactic medium. The ^{10}Be isotope is a radioactive nucleus that decays to ^{10}B in ~ 1.4 Myr, comparable to the cosmic-ray diffusion time scales in the Galaxy, while on the other hand, ^9Be is a stable nucleus. Therefore, ^{10}Be can be used as a cosmic clock to study the $^{10}\text{Be}/^9\text{Be}$ flux ratio and estimate the size of the Galactic halo (L) with higher precision. The Li/C ratio is analogous to the B/C flux ratio and is an excellent cross-check of the grammage X traversed by the cosmic-ray nuclei. Nevertheless, both the astrophysical parameters are currently dominated by the uncertainties of the nuclear fragmentation cross-sections and require precise cross-section measurements. The Li and Be fragments produced in $^{12}\text{C}+p$ reaction at 13.5A GeV/c were recorded by NA61/SHINE during the pilot run in 2018. The isotopic production cross-sections are extracted from a fit to the fragment distribution for Li and Be isotopes in the MTPC, and can be used for Galactic cosmic-ray propagation studies. Despite the low statistics, our preliminary fits exhibit suitable isotope identification for Li and Be fragments. The final step is to correct the calculated cross-section measurements and to estimate the systematic uncertainties.

Estimates of anti-deuteron production (GCR): Following the measurement of the deuteron signal, the negatively charged tracks were also analyzed. About $5 \cdot 10^4$ anti-protons were identified by the preliminary application of the *tof* – dE/dx analysis framework described earlier. Figure 34 (*left*) shows an example kinematic phase space bin where anti-protons, K^- , π^- , and electrons can be identified. For the same collision system, anti-deuteron production is about ~ 1000 times smaller than anti-proton production [74]. Applying this to all measurable phase space bins leads to an expectation of about 50 anti-deuterons in the existing $p+p$ 158 GeV/ c data sets. Figure 34 (*right*) shows a $p+p$ collision event with an anti-deuteron candidate. After carefully considering detector effects with simulations, the first anti-deuteron production cross-section measurements in $p+p$ at $p_{\text{Lab}} \approx 100$ GeV/ c will be performed in the next step.

6. Beam request for 2024 and plans for 2025

The first NA61/SHINE beam request for 2021–2024 was submitted to the SPSC in 2018 [76]. The Committee subsequently recommended it [77], and the Research Board approved the data taking in 2021 [78]. Due to the COVID-19 pandemic, the schedule of accelerators and the detector upgrade has been modified. In particular, the data taken with the T2K long target and the Pb beams for the open charm program and nuclear fragmentation cross-section measurements did not occur in 2021.

Moreover, the requested Pb beam time was reduced to two weeks in 2022 and four weeks in 2023. In addition to the primary Pb beam, the primary oxygen beam is planned for 2024. Finally, the post-LS2 data-taking period was extended to 2025. In 2022, NA61/SHINE submitted to SPSC two documents related to the post-LS2 beam request. The first one [79] modifies the Pb beam request for the open charm measurements, assuming that the Pb beam will also be available in 2025. The second document [80] presents the arguments and a detailed request for the oxygen beam in 2024 to study the diagram of high-energy nuclear collisions and for nuclear fragmentation cross-section measurements.

The revised data-taking schedule presented below takes the above into account and assumes that the data-taking conditions are as in Ref. [76]. Note that the number of collected events in a fixed time period is proportional to the duty cycle. Thus, it is critical to have it as high as possible.

6.1. Beam request for 2024

Test with primary oxygen beam:

- (i) **June/July 2024:** four days of primary oxygen beam at 13A GeV/ c for tests related to the post-LS3 measurements with light ion beams and measurements of nuclear fragmentation cross-section with light ion beams [2, 80].

Physics with proton beam:

- (i) **July – mid-August 2024:** four weeks of the secondary proton beam at 120 GeV/c for measurements of hadron emission from the DUNE replica target [76].

PSD calibration period and LHT test:

- (i) **September 2024:** two weeks of hadron beam at different momenta for the PSD calibration and liquid hydrogen target test.

Physics with lead beams:

- (i) **October 2024:** one week of a secondary (fragmented) light-ion beam at 13A GeV/c for nuclear fragmentation cross-section measurements. For details, see Ref. [81] and further details given in Appendix A. Note that the request is compatible with the goals of the charm program; see Sec. 2.3 for details.
- (ii) **October 2024:** three weeks of Pb beam at 150A GeV/c for charm hadron measurements in Pb+Pb collisions. For details, see Ref. [79].

Note that the requested Pb beam time refers to the effective beam time for NA61/SHINE and not to the calendar time of the Pb beam period; see Sec. 2.3 for details.

6.2. Plans for measurements in 2025

Physics with lead beams:

The measurements requested for 2025 are a continuation of open charm measurements with lead beams requested for the Run 3 period. Assuming successful 2024 ion data collection, we expect to request four weeks of Pb beam at 150A GeV/c to complete the program of charmed hadron measurements in Pb+Pb collisions. For details, see Refs. [79] and [81].

Physics with hadron beams:

NA61/SHINE is considering requesting hadron beams in the summer of 2025. Two types of measurements are discussed for neutrino, cosmic-ray, and strong interaction physics. Measurements with the low-energy hadron beams discussed in Addendum [82] and measurements with the proton beam at 300 GeV/c; for details, see Appendix B. The former requires the construction and commissioning of the low-energy branch of the H2 beam line, and the latter requires the construction and commissioning of the MRPC time-of-flight detector located on the Saleve side of the experiment.

7. Summary

This NA61/SHINE annual report briefly presents the status and plans of the NA61/SHINE experiment [1] at the CERN SPS. The report refers to the period November 2022 – October 2023.

The summary of this report is as follows:

- (I) In November 2022, the NA61/SHINE experiment received a 150A GeV/c Pb beam, initiating data recording on charm production in Pb+Pb. We gathered 30 million Pb+Pb interactions over a week, marking the first lead ion beam measurement after a hardware upgrade during Long Shutdown 2 (see Section 2). In the 2023 Pb+Pb data-taking period, the total number of recorded Pb+Pb interactions amounts to 150 million (see Section 2).
- (II) NA61/SHINE collected data with secondary hadron beams for six weeks in July and August 2023 (see Section 2). The first four weeks of the period were devoted to 60 GeV/c K^+ +C interactions, and the remaining two weeks to 120 GeV/c proton interactions on Ti and C. A total of 383 million events were collected during this run.
- (III) The detector upgrade completed in 2022 (see Section 3) assumed an increase of the data-taking rate to about 1 kHz. The physics runs unequivocally confirmed the successful attainment of the upgrade's primary objective. The data-taking rate soared to a maximum of 1.6 kHz for low multiplicity hadron-induced reactions, and it is about 1.2 kHz for Pb+Pb collisions.
- (IV) The reconstruction and calibration software is continuously maintained and developed (see Section 4). The new structure of the calibration database has been recently revised and modified. Now, it contains new and upgraded sub-detectors. Also, dedicated software managers, the tools responsible for reading information from the database, were revised or prepared from scratch. The new calibration software tools were implemented and used for data collected by the upgraded detector. The calibration procedure for data collected in 2022 is advanced, especially for TPCs and Vertex Detector.
- (V) New physics results, final and preliminary, were released (see Section 5):

Results relevant for the NA61/SHINE study of the onsets of deconfinement and fire-ball and search for the critical point include:

- (a) femtoscopy analysis in 0–20% central Be+Be collisions at 150A GeV/c,
- (b) proton intermittency in Ar+Sc collisions at 150A GeV/c,
- (c) π^\pm , K^\pm , p , and \bar{p} production in 0–10% central Ar+Sc collisions at 13A–150A GeV/c,
- (d) π^- , K^+ , and K^- production in 0–20% central Xe+La collisions at 150A GeV/c,
- (e) K_S^0 production in inelastic $p+p$ collisions at 31 and 40 GeV/c,
- (f) K_S^0 production in 0–10% central Ar+Sc collisions at 75A GeV/c,
- (g) Λ production in 0–10% central Ar+Sc collisions at 75A GeV/c.

The recent results obtained within the NA61/SHINE experiment for long-baseline neutrino oscillation experiments and cosmic-ray experiments include:

- (a) neutral hadrons from $p+C$ at 120 GeV/c interactions,
- (b) charged hadrons from $p+C$ at 120 GeV/c interactions,
- (c) production of boron isotopes in $^{12}\text{C}+p$ at 13.5A GeV/c.

(VI) The requested beam periods in 2024 are presented in Section 6.1. They include tests with a primary oxygen beam, physics data taking with a secondary proton beam, hadron beams for PSD calibration and LHT test, and physics data taking with lead beams. The latter includes three weeks for open charm production in Pb+Pb collisions at $150A$ GeV/ c and one week with a secondary ion beam (fragmented Pb beam) at $13A$ GeV/ c for the galactic cosmic-ray physics. The planned lead and hadron beam periods in 2025 are discussed in Section 6.2.

Note that the Pb beam time refers to the effective time for NA61/SHINE and not to the calendar duration of the Pb period; see Sec. 2.3 for details.

Acknowledgments

We would like to thank the CERN EP, BE, HSE and EN Departments for the strong support of NA61/SHINE.

This work was supported by the Hungarian Scientific Research Fund (grant NKFIH 138136/137812/138152 and TKP2021-NKTA-64), the Polish Ministry of Science and Higher Education (DIR/WK/2016/2017/10-1, WUT ID-UB), the National Science Centre Poland (grants 2014/14/E/ST2/00018, 2016/21/D/ST2/01983, 2017/25/N/ST2/02575, 2018/29/N/ST2/02595, 2018/30/A/ST2/00226, 2018/31/G/ST2/03910, 2019/33/B/ST9/03059, 2020/39/O/ST2/00277), the Norwegian Financial Mechanism 2014–2021 (grant 2019/34/H/ST2/00585), the Polish Minister of Education and Science (contract No. 2021/WK/10), the European Union’s Horizon 2020 research and innovation programme under grant agreement No. 871072, the Ministry of Education, Culture, Sports, Science and Technology, Japan, Grant-in-Aid for Scientific Research (grants 18071005, 19034011, 19740162, 20740160 and 20039012,22H04943), the German Research Foundation DFG (grants GA 1480/8-1 and project 426579465), the Bulgarian Ministry of Education and Science within the National Roadmap for Research Infrastructures 2020–2027, contract No. D01-374/18.12.2020, Serbian Ministry of Science, Technological Development and Innovation (grant OI171002), Swiss Nationalfonds Foundation (grant 200020117913/1), ETH Research Grant TH-01 07-3, National Science Foundation grant PHY-2013228 and the Fermi National Accelerator Laboratory (Fermilab), a U.S. Department of Energy, Office of Science, HEP User Facility managed by Fermi Research Alliance, LLC (FRA), acting under Contract No. DE-AC02-07CH11359 and the IN2P3-CNRS (France).

The data used in this paper were collected before February 2022.

A. Nuclear fragmentation measurements for Galactic cosmic-ray physics

In this section, we provide further input on the impact of measurements of nuclear fragmentation cross-sections with NA61/SHINE, as requested by the SPSC referees. These measurements are part of the physics program of the collaboration for Run 3, as detailed in Ref. [81], and the LS2 upgrade of the detector was partially funded to perform these measurements. A pilot run [83] on fragmentation measurements with NA61/SHINE was successfully completed in 2018. First results have been presented at conferences [64–66] demonstrating the unique capabilities of NA61/SHINE and the SPS to provide precise measurements of nuclear fragmentation cross-sections at high energies ($> 10A$ GeV). The original beam request for 24 days of secondary light-ion beam at $13A$ GeV/ c with a zero-bias trigger from Ref. [81] has been adapted to one week of data taking with a minimum bias trigger to account for the reduced overall availability of the Pb-beam time.

A.1. Motivation

Space-based detectors like AMS, CALET, and DAMPE have recently collected a wealth of new data on Galactic cosmic rays, e.g. Refs. [61–63, 84–98]. The fluxes of leptons, nuclei, and anti-protons from GeV to TeV are now known to an unprecedented percent-level precision. These new data sets provide a unique diagnostic of cosmic-ray propagation in the Galaxy and an opportunity to find signatures of dark matter annihilation in the Galaxy, see e.g. Refs. [99–102].

Cosmic rays can be classified as being of primary or secondary origin. Primary cosmic-ray nuclei are assumed to be accelerated in supernova remnants (e.g., p , He, C, N, O, Fe). In contrast, secondary cosmic rays are created in nuclear interactions of primary cosmic rays with protons and helium nuclei of the interstellar medium (e.g., e^+ , \bar{p} , d, Li, Be, B). The flux ratios of secondary to primary cosmic rays are key observables to determine the characteristics of the propagation of cosmic rays in the Galaxy, such as the effective diffusion coefficient and its energy dependence, the column depth of material traversed by cosmic rays, and the size of the magnetic halo of the Galaxy.

Unfortunately, the interpretation of these secondary to primary ratios is severely hampered by uncertainties in the modeling of the propagation of cosmic rays in the Galaxy due to uncertainties in the cross-sections of nuclear fragmentation on the level of 10–20% [103–107]. These uncertainties propagate directly to the flux predictions of astrophysical anti-matter and the signal prediction of particle fluxes from astrophysical dark matter annihilation in the Galactic halo. Whereas many measurements exist at low energies, there is a particular need to measure cross-sections at high energies above the nuclear resonances ($\gtrsim 10A$ GeV/ c), where the cross-sections are expected to reach their asymptotic values. A precise measurement of all relevant fragmentation channels in this energy range can, therefore, drastically improve the uncertainties of cosmic-ray propagation over the whole energy range accessible to modern space-based cosmic-ray experiments.

Table 2: Required number of interactions of different nuclei with protons to be recorded, as estimated in Ref. [108]. The cumulative number of required interactions is quoted in the bottom row.

reaction	N_{int}	reaction	N_{int}
$^{16}\text{O}+p$	60k	$^{28}\text{Si}+p$	50k
$^{12}\text{C}+p$	50k	$^{24}\text{Mg}+p$	50k
$^{11}\text{B}+p$	10k	$^{20}\text{Ne}+p$	50k
$^{15}\text{N}+p$	10k	$^{22}\text{Ne}+p$	20k
$^{14}\text{N}+p$	10k	$^{27}\text{Al}+p$	10k
$^{10}\text{B}+p$	5k	$^{26}\text{Mg}+p$	10k
$^{13}\text{C}+p$	5k	$^{23}\text{Na}+p$	10k
$^7\text{Li}+p$	5k	$^{25}\text{Mg}+p$	10k
		$^{21}\text{Ne}+p$	10k
		$^{32}\text{S}+p$	5k
		$^{29}\text{Si}+p$	5k
$\Sigma N_{\text{int}} = 3.8 \times 10^5$			

A.2. Impact of measurements by NA61/SHINE

Triggered by the request of the SPSC referees to quantify the impact of new cross-section measurements, a new study was performed in Ref. [108] focusing on the key questions addressed by the CR community, the derivation of cosmic-ray transport parameters and their impact on indirect dark matter searches. To assess the improvement brought by future nuclear cross-section measurements with NA61/SHINE, mock cross-section models smeared with different uncertainties were created and subsequently used to fit the transport parameters on the secondary to primary ratios. In that way, an ensemble of cosmic-ray transport parameters was obtained that could be used to propagate the cross-section uncertainty into predictions like the anti-proton flux or the derivation of the size of the Galactic halo.

The calculated uncertainties are based on the estimated precision of future measurements from NA61/SHINE as shown in Tab. 2, where the number of required *interactions* with a proton target is listed. The intent is to follow the same strategy as in the pilot run and use a combination of carbon and polyethylene targets to derive the fragmentation on protons. Therefore, the effective number of interactions to be recorded will be at least four times larger. In total, more than 400k interactions of projectiles up to Si with protons need to be recorded, and therefore, at least 2M interactions in total. All of the projectiles listed in the table can be obtained from a fragmented Pb beam with a single setting of the H2 beam line to $A/Z = 2$ ions since our experience from the pilot run shows that the few required ions with $A/Z \neq 2$ will be present in the beam due to the Fermi motion of the Pb fragments. Given the statistics collected during the data taking with the upgraded NA61/SHINE detector in 2022 and 2023, the required statistics of interactions can be recorded within the requested one week of data taking, cf. Sec. 6, and allow for a substantial control sample of pre-scaled zero bias triggers and data taking with different magnetic field settings to minimize the systematic uncertainties of the measurement.

Given such a data set of interactions of secondary Pb fragments with protons, the expected

improvement of the cosmic-ray propagation parameters is displayed in Fig. 35. The two parameters shown are the relative uncertainty of the normalization of the diffusion coefficient, D_0 , and the spectral index, δ (energy dependence $D(E) = D_0(E/Z)^\delta$, where Z denotes the cosmic-ray charge). As can be seen, the current uncertainties due to the limited knowledge of cross-sections (red contours) are much larger than the ones originating from the uncertainty of the cosmic-ray data (black contours). Once the data from NA61/SHINE is available (dashed blue lines), the uncertainty will be close to the uncertainty originating from the precision of the measurements of cosmic-ray experiments. The improvement is shown for four secondary-to-primary ratios: Li/C, Be/C, B/C, and F/Si. Ideally, each of these could be a tracer of the cosmic-ray propagation. However, at the moment, the interpretation of the different ratios yields different propagation parameters. This is known as the “Lithium excess” and the “Fluorine anomaly” [109–114]. Only if the cross-section uncertainties result in D_0 uncertainties at the level of the blue curves in Fig. 35, will it be possible to investigate these newly discovered anomalies and their potential impact on our understanding of stellar nucleosynthesis and cosmic-ray propagation.

Concerning the prediction of the flux of astrophysical anti-protons, the expected improvements are shown in Fig. 36 that shows the residual of the AMS data to the prediction of Ref. [115]. As can be seen, data and theory agree currently well within the large uncertainties of cosmic-ray propagation (red band). Only after the intended fragmentation measurements from NA61/SHINE are available can the model uncertainties be reduced to the level at which deviations due to astrophysical dark matter can be searched for.

Finally, the impact of the proposed measurements on determining the size of the Galactic halo L is shown in Fig. 37. The value of L can be estimated from the analysis of “cosmic-ray clocks”, i.e., secondary nuclei that are unstable on astrophysical time scales (e.g., ^{10}Be with a lifetime of 1.6 Myr) and again, the current uncertainties shown in red exceed by far the precision of the data, see also Ref. [116]. With the measurements proposed to be performed in 2024, this uncertainty would become smaller than the current data uncertainty (to be soon improved by, e.g., the HELIX balloon experiment [117]). The size of the Galactic halo is of intrinsic astrophysical interest to understand the origin of magnetism in the Milky Way. Moreover, uncertainties in L directly propagate to predictions of the flux of anti-particles produced by astrophysical dark matter in the halo.

In summary, new measurements of fragmentation cross-sections with NA61/SHINE will significantly impact our understanding of the propagation of cosmic rays in the Galaxy. We estimate that the current error on the normalization of the diffusion coefficient will shrink from $\geq 30\%$ to 5–10%. Correspondingly, the propagation-related uncertainty of astrophysical anti-protons will be reduced from $\sim 15\%$ to $< 5\%$. The proposed measurements are essential to reach the full physics potential of high-precision data from space-based cosmic-ray experiments. To our knowledge, NA61/SHINE and the SPS are worldwide the only facilities that allow for this measurement at a beam momenta higher than $10A \text{ GeV}/c$.

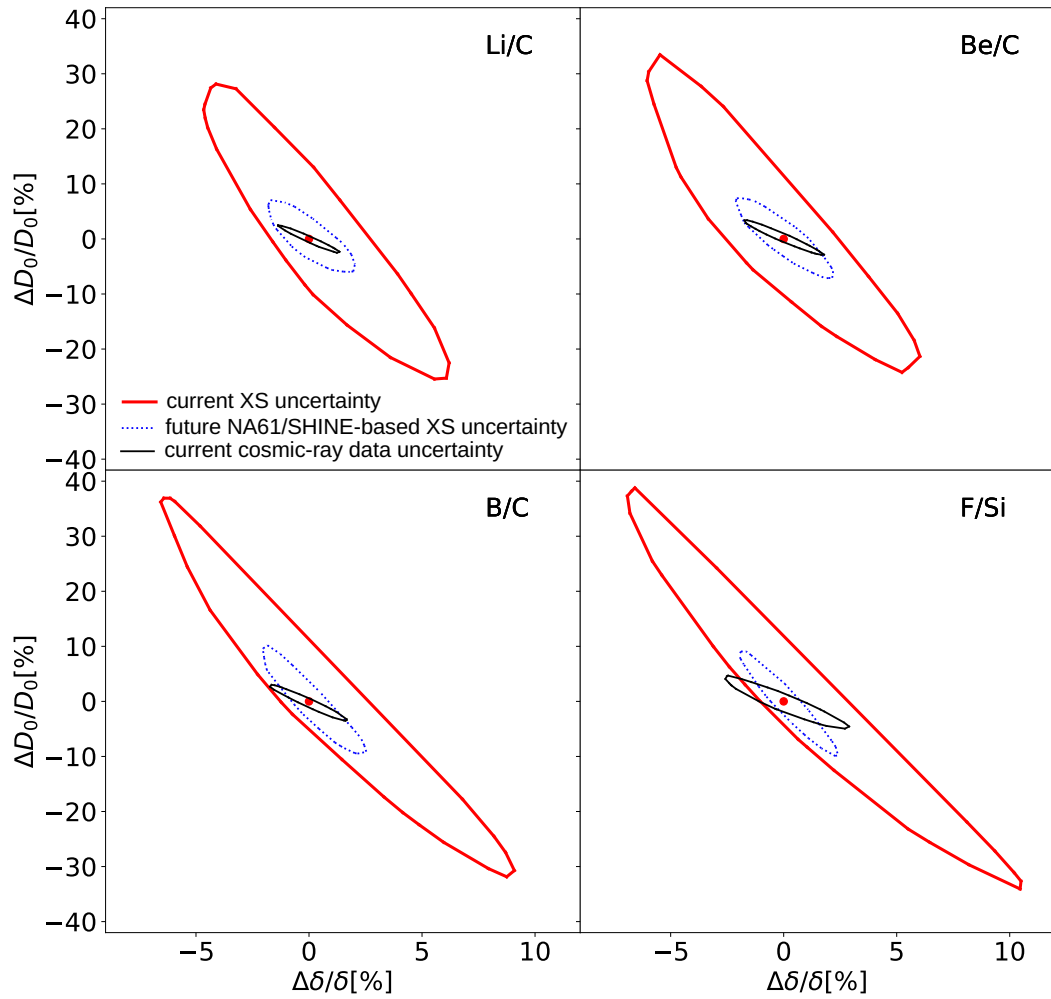


Figure 35: Forecast of accuracy on the determination of transport parameters after the proposed measurement of nuclear fragmentation with NA61/SHINE. Each figure shows 1σ contours in the (D_0, δ) relative error plane derived for four different secondary-to-primary ratios: Li/C, Be/C, B/C and F/Si. The current uncertainties due to fragmentation cross-section are shown as red contours. The estimated uncertainties based on future NA61/SHINE measurements are shown as dashed blue contours. The uncertainty arising from the precision of the cosmic-ray data is shown as a solid black contour. Adapted from Ref. [108].

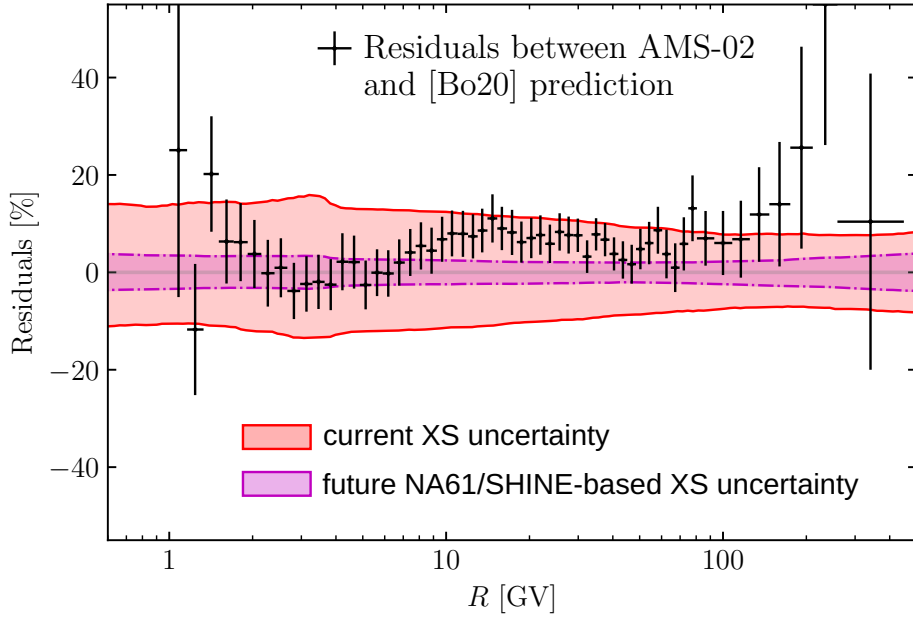


Figure 36: Forecast of accuracy on the predicted \bar{p} flux after the proposed measurement of nuclear fragmentation with NA61/SHINE. The red envelope shows the current ‘transport’ uncertainty, i.e. uncertainty related to the transport parameter uncertainties (linked to the nuclear cross-section uncertainties). The magenta envelopes show the estimated uncertainty after new cross-section measurements with NA61/SHINE. With this improvement, the uncertainty is smaller than the current AMS data uncertainties [98]. The symbols show the residuals of the data with regard to the best-fit \bar{p} prediction of Ref. [115] ([Bo20] in the legend), and the x -axis gives the cosmic-ray rigidity $R = E/Z$ (energy E , charge Z). Adapted from Ref. [108].

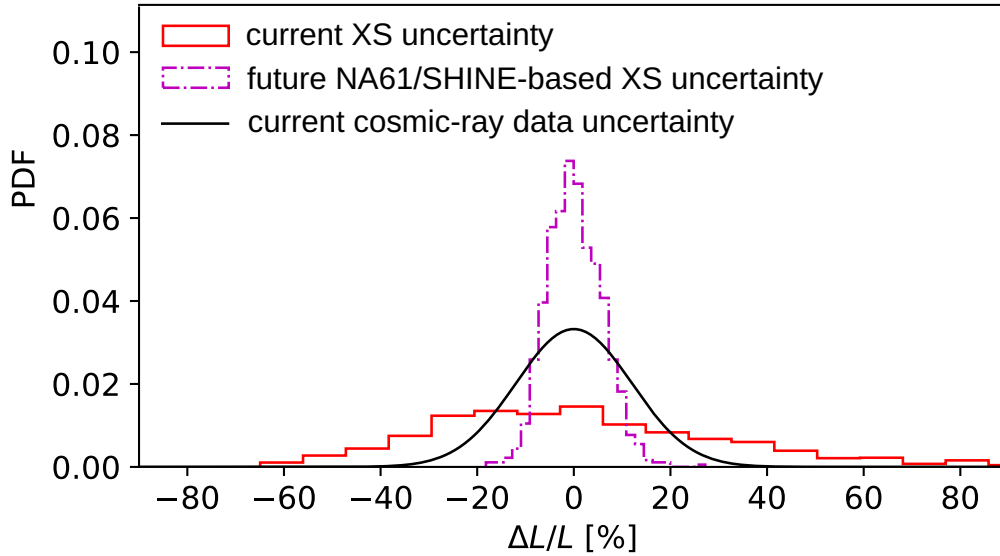


Figure 37: The relative precision of the halo size L of the Galaxy. The red line shows the current uncertainty on L , and the magenta line shows the reduced uncertainty as expected after future cross-section measurements with NA61/SHINE. With this improvement, the uncertainty related to cross-sections becomes smaller than the current experimental uncertainties (as estimated in Ref. [118]). Adapted from Ref. [108].

B. High-statistics measurements of $p+p$ interactions for cosmic-ray and strong interaction physics

NA61/SHINE considers requesting proton beam at 300 GeV/ c . This is motivated by multiple thrusts (a dedicated addendum is in preparation):

- (i) Cosmic-ray anti-deuterons potentially open the window to new transformative fields in particle astrophysics and beyond, e.g., the nature of dark matter (for a review, see Ref. [72]). The impact of new-physics searches with anti-deuterons can be increased by reducing uncertainties related to anti-deuteron production cross-sections of cosmic rays with the interstellar medium. These uncertainties are at a factor of 10 in the most critical energy region [73, 74, 119]. Especially $p+p$ data at about $p = 50 - 400$ GeV/ c from modern experiments is lacking. The upgraded NA61/SHINE detector can, for the first time, precisely measure anti-deuteron production in $p+p$ interactions in this energy range and significantly contribute to a new physics search. Measuring a very small cross-section like the anti-deuteron production particularly benefits from the upgraded detector and the extended data-taking period. Something that was not feasible before.
- (ii) Strangeness production provides input to understanding particle production mechanisms in high-energy collisions and provides the ultimate information on creating large clusters of strongly interacting matter. The strangeness enhancement [120] is one of the basic signatures of a quark-gluon plasma signal in nucleus-nucleus collisions. It was determined experimentally [121, 122] and found to increase with the strangeness content of the studied particle [123, 124]. However, experimental results on enhancement (especially for heavier baryons) are only available for the highest SPS and RHIC and for LHC energies. Measurements with NA61/SHINE using a hadron beam at 300 GeV/ c will connect these measurements.
- (iii) Strangeness enhancement cannot deliver information on the order of the phase transition. Fluctuations, defined through higher-order moments and cumulants of the multiplicity and net-charge distributions, are believed to be a suitable tool for it [125]. Search for the predicted critical point of strongly interacting matter is of particular interest [19, 125–130]. It was already addressed by the system size and energy scan of NA61/SHINE performed before LS2 [10, 19, 131]. Currently, none of the reported results of NA61/SHINE indicates its presence. However, the STAR experiment reported a non-monotonic behavior of net-baryon fluctuation quantities in Au+Au collisions [132]. In realistic high-energy collisions, fluctuations are also sensitive to numerous other effects, such as detector efficiency, acceptance, feed-down, or centrality determination. Some of these effects can be estimated in $p+p$ collisions, a reference reaction for nucleus-nucleus collisions. Before LS2 NA61/SHINE collected data on $p+p$ interactions at six beam momenta (20, 31, 40, 80, 158, and 400 GeV/ c) [131, 133, 134]. This new data set would cover the gap between these measurements and provide a reference for nucleus-nucleus collisions.

References

- [1] N. Antoniou *et al.*, [NA61/SHINE Collab.], “Study of Hadron Production in Hadron-Nucleus and Nucleus-Nucleus Collisions at the CERN SPS,” Tech. Rep. CERN-SPSC-2006-034, SPSC-P-330, CERN, Geneva, 2006. <https://cds.cern.ch/record/995681>.
- [2] H. Adhikary *et al.*, [NA61/SHINE Collab.], “Addendum to the NA61/SHINE Proposal: Request for light ions beams in Run 4,” Tech. Rep. CERN-SPSC-2023-022, SPSC-P-330-ADD-14, CERN, Geneva, 2023. <https://cds.cern.ch/record/2867952>.
- [3] H. Adhikary *et al.*, [NA61/SHINE Collab.], “Report from the NA61/SHINE experiment at the CERN SPS,” Tech. Rep. CERN-SPSC-2022-034, SPSC-SR-319, CERN, Geneva, 2022. <https://cds.cern.ch/record/2839856>.
- [4] M. Bajda “Development of track reconstruction for the upgraded NA61/SHINE Vertex Detector,” MSc thesis CERN-THESIS-2023-120, Jagiellonian University, 2023. <https://cds.cern.ch/record/2867131>.
- [5] [NA61/SHINE Collab.], “Technical Design Reports for the upgrade of NA61/SHINE detector subsystems,” Tech. Rep. NA61-PUBLIC, CERN, Geneva, 2020. <https://edms.cern.ch/document/2422986/1>.
- [6] G. Rinella, [ALICE Collab.] *Nucl. Instrum. Meth.* **A845** (2017) 583.
- [7] M. Gazdzicki, M. Gorenstein, and P. Seyboth *Int.J.Mod.Phys.* **E23** (2014) 1430008, arXiv:1404.3567 [nucl-ex].
- [8] A. Aduszkiewicz *et al.*, [NA61/SHINE Collab.], “Report from the NA61/SHINE experiment at the CERN SPS,” Tech. Rep. CERN-SPSC-2017-038, SPSC-SR-221, CERN, Geneva, 2017. <http://cds.cern.ch/record/2287091>.
- [9] T. Csorgo, S. Hegyi, and W. A. Zajc *Eur. Phys. J. C* **36** (2004) 67–78, arXiv:nucl-th/0310042.
- [10] H. Adhikary *et al.*, [NA61/SHINE Collab.] *Eur. Phys. J. C* **83** no. 10, (2023) 919, arXiv:2302.04593 [nucl-ex].
- [11] T. Csorgo, S. Hegyi, T. Novak, and W. A. Zajc *AIP Conf. Proc.* **828** no. 1, (2006) 525–532, arXiv:nucl-th/0512060.
- [12] B. Porfy, [NA61/SHINE Collab.] *Universe* **9** no. 7, (2023) 298, arXiv:2306.08696 [nucl-ex].
- [13] A. Adare *et al.*, [PHENIX Collab.] *Phys. Rev. C* **97** no. 6, (2018) 064911, arXiv:1709.05649 [nucl-ex].
- [14] R. Vertesi, T. Csorgo, and J. Sziklai *Phys. Rev. C* **83** (2011) 054903, arXiv:0912.0258 [nucl-ex].
- [15] B. I. Abelev *et al.*, [STAR Collab.] *Phys. Rev. C* **80** (2009) 024905, arXiv:0903.1296 [nucl-ex].
- [16] H. Beker *et al.*, [NA44 Collab.] *Phys. Rev. Lett.* **74** (1995) 3340–3343.
- [17] C. Alt *et al.*, [NA49 Collab.] *Phys. Rev. C* **77** (2008) 064908, arXiv:0709.4507 [nucl-ex].
- [18] Y. M. Sinyukov *Nucl. Phys. A* **566** (1994) 589C–592C.
- [19] H. Adhikary *et al.*, [NA61/SHINE Collab.] *Eur. Phys. J. C* **83** no. 9, (2023) 881, arXiv:2305.07557 [nucl-ex].
- [20] K. Werner *Nucl. Phys. Proc. Suppl.* **175-176** (2008) 81–87.
- [21] T. Pierog and K. Werner *Nucl.Phys.Proc.Suppl.* **196** (2009) 102–105, arXiv:0905.1198 [hep-ph].
- [22] H. Adhikary *et al.*, [NA61/SHINE Collab.] arXiv:2308.16683 [nucl-ex].
- [23] P. Podlaski, “NA61/SHINE Overview,” in *30th International Conference on Ultra-relativistic Nucleus-Nucleus Collisions (Quark Matter 2023)*. 2023. <https://indico.cern.ch/event/1139644/contributions/5343986>.

- [24] O. Panova, “First results on spectra of identified hadrons in central Xe+La collisions from NA61/SHINE at CERN SPS,” in *30th International Conference on Ultra-relativistic Nucleus-Nucleus Collisions (Quark Matter 2023)*. 2023. <https://indico.cern.ch/event/1139644/contributions/5514531>.
- [25] N. Abgrall *et al.*, [NA61/SHINE Collab.] *Eur. Phys. J. C* **74** no. 3, (2014) 2794, arXiv:1310.2417 [hep-ex].
- [26] M. Gazdzicki and A. Rybicki, [NA61/SHINE Collab.] *Acta Phys. Polon. B* **50** (2019) 1057–1070.
- [27] A. Bialas, M. Bleszynski, and W. Czyz *Nucl. Phys.* **B111** (1976) 461.
- [28] E. Andronov, M. Kuich, and M. Gaździcki *Universe* **9** no. 2, (2023) 106, arXiv:2205.06726 [hep-ph].
- [29] M. Cirkovic, “News from the NA61/SHINE,” in *NICA Days 2023 and XII Collaboration Meeting of the MPD Experiment at the NICA Facility, Belgrade, Serbia*. 2023. <https://indico.jinr.ru/event/3746>.
- [30] R. L. Workman *et al.*, [Particle Data Group Collab.] *PTEP* **2022** (2022) 083C01.
- [31] A. Acharya *et al.*, [NA61/SHINE Collab.] *Eur. Phys. J. C* **82** no. 1, (2022) 96, arXiv:2106.07535 [hep-ex].
- [32] M. Cirkovic, “ K_S^0 production in $p+p$ interactions measured by NA61/SHINE,” in *The 11th Conference of the Balkan Physical Union (BPU11 Congress)*. 2022. <https://indico.bpu11.info/event/1/contributions/281>.
- [33] W. Brylinski, “Large isospin symmetry violation in kaon production?,” in *30th International Conference on Ultra-relativistic Nucleus-Nucleus Collisions (Quark Matter 2023)*. 2023. <https://indico.cern.ch/event/1139644/contributions/5541473>.
- [34] P. B. Pal, “An introductory course of particle physics”, CRC Press, Taylor & Francis Group (2015).
- [35] I. Smushkevich, Dokl. Akad. Nauk SSSR 103 (1955), 235.
- [36] C. G. Wohl, Am. J. Phys. 50 (1982) 748–753.
- [37] A. J. MacFarlane, G. Pinski, and G. Sudarshan *Phys. Rev.* **140** (1965) B1045.
- [38] V. Vovchenko and H. Stoecker *Comput. Phys. Commun.* **244** (2019) 295–310, arXiv:1901.05249 [nucl-th].
- [39] W. Brylinski, M. Gazdzicki, F. Giacosa, M. Gorenstein, R. Poberezhnyuk, S. Samanta, and H. Stroebele, private communication, paper in preparation.
- [40] Y. Balkova, “Probing the onset of deconfinement: recent results from the NA61/SHINE experiment,” in *International school of nuclear physics, 44th Course: From quarks and gluons to hadrons and nuclei Erice, Sicily*. 2023. <http://crunch.ikp.physik.tu-darmstadt.de/erice/2023>.
- [41] V. V. Ammosov *et al.* *Nucl. Phys. B* **115** (1976) 269–286.
- [42] C. Alt *et al.*, [NA49 Collab.] *Phys. Rev. C* **78** (2008) 034918, arXiv:0804.3770 [nucl-ex].
- [43] M. Gazdzicki and D. Roehrich *Z.Phys.* **C65** (1995) 215.
- [44] S. V. Afanasiev *et al.*, [NA49 Collab.] *Phys. Rev. C* **66** (2002) 054902, arXiv:nucl-ex/0205002.
- [45] P. Adamson *et al.* *Nucl. Instrum. Meth. A* **806** (2016) 279–306, arXiv:1507.06690 [physics.acc-ph].
- [46] D. A. Harris and S. Kopp, [MINERvA Collab.] *AIP Conf. Proc.* **1382** no. 1, (2011) 179–181.
- [47] P. N. Shanahan and P. L. Vahle, [NOvA Collab.] *Eur. Phys. J. ST* **230** no. 24, (2021) 4259–4273.
- [48] B. Rumberger *et al.* *JINST* **15** no. 07, (2020) P07013, arXiv:2004.11358 [physics.ins-det].
- [49] L. Aliaga *et al.*, [MINERvA Collab.] *Phys. Rev. D* **94** no. 9, (2016) 092005, arXiv:1607.00704 [hep-ex]. [Addendum: Phys.Rev.D 95, 039903 (2017)].
- [50] H. Adhikary *et al.*, [NA61/SHINE Collab.] *Phys. Rev. D* **107** no. 7, (2023) 072004, arXiv:2211.00183 [hep-ex].

- [51] H. Adhikary *et al.*, [NA61/SHINE Collab.] *Phys. Rev. D* **108** no. 7, (2023) 072013, arXiv:2306.02961 [hep-ex].
- [52] A. Acharya *et al.*, [NA61/SHINE Collab.], “Report from the NA61/SHINE experiment at the CERN SPS,” Tech. Rep. CERN-SPSC-2021-027, SPSC-SR-298, CERN, Geneva, 2021. <https://cds.cern.ch/record/2783036>.
- [53] H. Adhikary *et al.*, [NA61/SHINE Collab.] *Phys. Rev. D* **107** no. 6, (2023) 062004, arXiv:2209.10561 [nucl-ex].
- [54] E.-J. Ahn, R. Engel, T. K. Gaisser, P. Lipari, and T. Stanev *Phys.Rev.* **D80** (2009) 094003, arXiv:0906.4113 [hep-ph].
- [55] S. Ostapchenko *Phys.Rev.* **D83** (2011) 014018, arXiv:1010.1869 [hep-ph].
- [56] T. Pierog, I. Karpenko, J. M. Katzy, E. Yatsenko, and K. Werner *Phys. Rev.* **C92** no. 3, (2015) 034906, arXiv:1306.0121 [hep-ph].
- [57] A. Fedynitch, F. Riehn, R. Engel, T. K. Gaisser, and T. Stanev *Phys. Rev. D* **100** no. 10, (2019) 103018, arXiv:1806.04140 [hep-ph].
- [58] A. Aduszkiewicz *et al.*, [NA61/SHINE Collab.] *Eur. Phys. J. C* **77** no. 9, (2017) 626, arXiv:1705.08206 [nucl-ex].
- [59] T. Pierog and K. Werner *Phys. Rev. Lett.* **101** (2008) 171101, arXiv:astro-ph/0611311 [astro-ph].
- [60] J. Albrecht *et al.* *Astrophys. Space Sci.* **367** no. 3, (2022) 27, arXiv:2105.06148 [astro-ph.HE].
- [61] M. Aguilar *et al.*, [AMS Collab.] *Phys. Rev. Lett.* **117** no. 23, (2016) 231102.
- [62] O. Adriani *et al.*, [CALET Collab.] *Phys. Rev. Lett.* **129** no. 25, (2022) 251103, arXiv:2212.07873 [astro-ph.HE].
- [63] F. Alemanno *et al.*, [DAMPE Collab.] *Sci. Bull.* **67** (2022) 2162–2166, arXiv:2210.08833 [astro-ph.HE].
- [64] M. Unger, [NA61/SHINE Collab.] *PoS ICRC2019* (2020) 446, arXiv:1909.07136 [astro-ph.HE].
- [65] N. Amin, [NA61/SHINE Collab.] *PoS ICRC2021* (2021) 102, arXiv:2107.12275 [nucl-ex].
- [66] N. Amin, [NA61/SHINE Collab.] *PoS ICRC2023* (2023) 075.
- [67] W. R. Webber, J. C. Kish, and D. A. Schrier *Phys. Rev. C* **41** (1990) 566–571.
- [68] W. R. Webber, A. Soutoul, J. C. Kish, J. M. Rockstroh, Y. Cassagnou, R. Legrain, and O. Testard *Phys. Rev. C* **58** (1998) 3539–3552.
- [69] W. R. Webber, J. C. Kish, J. M. Rockstroh, Y. Cassagnou, R. Legrain, A. Soutoul, O. Testard, and C. Tull *Astrophys. J.* **508** no. 2, (1998) 940–948.
- [70] W. R. Webber, J. C. Kish, J. M. Rockstroh, Y. Cassagnou, R. Legrain, A. Soutoul, O. Testard, and C. Tull *Astrophys.J.* **508** no. 2, (1998) 949–958.
- [71] C. Evoli, R. Aloisio, and P. Blasi *Phys. Rev.* **D99** no. 10, (2019) 103023, arXiv:1904.10220 [astro-ph.HE].
- [72] P. von Doetinchem *et al.* *JCAP* **08** (2020) 035, arXiv:2002.04163 [astro-ph.HE].
- [73] D.-M. Gomez-Coral, A. Menchaca Rocha, V. Grabski, A. Datta, P. von Doetinchem, and A. Shukla *Physical Review D* **98** no. 2, (2018) 023012, arXiv:1806.09303 [astro-ph.HE].
- [74] A. Shukla, A. Datta, P. von Doetinchem, D.-M. Gomez-Coral, and C. Kanitz *Phys. Rev. D* **102** no. 6, (2020) 063004, arXiv:2006.12707 [astro-ph.HE].
- [75] A. Shukla “Light nuclei and antinuclei production in proton-proton interactions,” PhD thesis CERN-THESIS-2023-051, University of Hawaii at Manoa, 2023. <https://cds.cern.ch/record/2859334>.

- [76] A. Aduszkiewicz *et al.*, [NA61/SHINE Collab.], “Reply to the SPSC questions on Addendum CERN-SPSC-2018-008 entitled Study of Hadron-Nucleus and Nucleus-Nucleus Collisions at the CERN SPS: Early Post-LS2 Measurements and Future Plans,” Tech. Rep. CERN-SPSC-2018-019, SPSC-P-330-ADD-11, CERN, Geneva, 2018. <https://cds.cern.ch/record/2621751>.
- [77] “Minutes of the 130th Meeting of the SPSC, Thursday and Friday, 7-8 June 2018,” Tech. Rep. CERN-SPSC-2018-020, SPSC-130, CERN, Geneva, 2018. <http://cds.cern.ch/record/2622174>.
- [78] “Minutes of the 232nd meeting of the Research Board, held on 11 March 2020,” Tech. Rep. CERN-DG-RB-2020-495, M-232, CERN, Geneva, 2020. <http://cds.cern.ch/record/2712812>.
- [79] [NA61/SHINE Collab.], “Open Charm Measurements: Pb-beam schedule and detector upgrade,” Tech. Rep. CERN-SPSC-2022-005, SPSC-M-792, CERN, Geneva, 2022. <https://cds.cern.ch/record/2799311>.
- [80] [NA61/SHINE Collab.], “Addendum to the NA61/SHINE Proposal: Request for oxygen beam in Run 3,” Tech. Rep. CERN-SPSC-2022-021, SPSC-P-330-ADD-13, CERN, Geneva, 2022. <https://cds.cern.ch/record/2810689>.
- [81] A. Aduszkiewicz *et al.*, [NA61/SHINE Collab.], “Study of Hadron-Nucleus and Nucleus-Nucleus Collisions at the CERN SPS: Early Post-LS2 Measurements and Future Plans,” Tech. Rep. CERN-SPSC-2018-008, SPSC-P-330-ADD-10, CERN, Geneva, 2018. <https://cds.cern.ch/record/2309890>.
- [82] A. Acharya *et al.*, [NA61/SHINE Collab.], “Addendum to the NA61/SHINE Proposal: A Low-Energy Beamline at the SPS H2,” Tech. Rep. CERN-SPSC-2021-028, SPSC-P-330-ADD-12, CERN, Geneva, 2021. <https://cds.cern.ch/record/2783037>.
- [83] A. Aduszkiewicz *et al.*, [NA61/SHINE Collab.], “Feasibility Study for the Measurement of Nuclear Fragmentation Cross Sections with NA61/SHINE at the CERN SPS,” Tech. Rep. CERN-SPSC-2017-035, SPSC-P-330-ADD-9, CERN, Geneva, 2017. <https://cds.cern.ch/record/2287004>.
- [84] M. Aguilar *et al.*, [AMS Collab.] *Phys. Rev. Lett.* **130** no. 21, (2023) 211002.
- [85] O. Adriani *et al.*, [CALET Collab.] *Phys. Rev. Lett.* **129** no. 10, (2022) 101102, arXiv:2209.01302 [astro-ph.HE].
- [86] O. Adriani *et al.*, [CALET Collab.] *Phys. Rev. Lett.* **128** no. 13, (2022) 131103, arXiv:2204.00845 [astro-ph.HE].
- [87] O. Adriani *et al.*, [CALET Collab.] *Phys. Rev. Lett.* **126** no. 24, (2021) 241101, arXiv:2106.08036 [astro-ph.HE].
- [88] M. Aguilar *et al.*, [AMS Collab.] *Phys. Rev. Lett.* **127** no. 2, (2021) 02101. [Erratum: *Phys.Rev.Lett.* **127**, 159901 (2021)].
- [89] M. Aguilar *et al.*, [AMS Collab.] *Phys. Rev. Lett.* **126** no. 8, (2021) 081102.
- [90] M. Aguilar *et al.*, [AMS Collab.] *Phys. Rev. Lett.* **126** no. 4, (2021) 041104.
- [91] M. Aguilar *et al.*, [AMS Collab.] *Phys. Rev. Lett.* **124** no. 21, (2020) 211102.
- [92] Q. An *et al.*, [DAMPE Collab.] *Sci. Adv.* **5** no. 9, (2019) eaax3793, arXiv:1909.12860 [astro-ph.HE].
- [93] M. Aguilar *et al.*, [AMS Collab.] *Phys. Rev. Lett.* **122** no. 10, (2019) 101101.
- [94] M. Aguilar *et al.*, [AMS Collab.] *Phys. Rev. Lett.* **122** no. 4, (2019) 041102.
- [95] M. Aguilar *et al.*, [AMS Collab.] *Phys. Rev. Lett.* **121** no. 5, (2018) 051103.
- [96] M. Aguilar *et al.*, [AMS Collab.] *Phys. Rev. Lett.* **120** no. 2, (2018) 021101.
- [97] O. Adriani *et al.*, [CALET Collab.] *Phys. Rev. Lett.* **119** no. 18, (2017) 181101, arXiv:1712.01711 [astro-ph.HE].
- [98] M. Aguilar *et al.*, [AMS Collab.] *Phys. Rev. Lett.* **117** no. 9, (2016) 091103.

- [99] A. W. Strong, I. V. Moskalenko, and V. S. Ptuskin *Ann. Rev. Nucl. Part. Sci.* **57** (2007) 285–327, [arXiv:astro-ph/0701517](#).
- [100] E. Amato and P. Blasi *Adv. Space Res.* **62** (2018) 2731–2749, [arXiv:1704.05696](#) [astro-ph.HE].
- [101] T. A. Porter, R. P. Johnson, and P. W. Graham *Ann. Rev. Astron. Astrophys.* **49** (2011) 155–194, [arXiv:1104.2836](#) [astro-ph.HE].
- [102] J. Lavallo and P. Salati *Comptes Rendus Physique* **13** (2012) 740–782, [arXiv:1205.1004](#) [astro-ph.HE].
- [103] W. R. Webber, A. Soutoul, J. C. Kish, and J. M. Rockstroh *ApJS* **144** no. 1, (2003) 153.
- [104] D. Maurin, A. Putze, and L. Derome *Astron. Astrophys.* **516** (2010) A67, [arXiv:1001.0553](#) [astro-ph.HE].
- [105] Y. Génolini, A. Putze, P. Salati, and P. D. Serpico *Astron. Astrophys.* **580** (2015) A9, [arXiv:1504.03134](#) [astro-ph.HE].
- [106] N. Tomassetti *Phys. Rev. D* **96** no. 10, (2017) 103005, [arXiv:1707.06917](#) [astro-ph.HE].
- [107] A. Reinert and M. W. Winkler *JCAP* **01** (2018) 055, [arXiv:1712.00002](#) [astro-ph.HE].
- [108] Y. Génolini, D. Maurin, I. V. Moskalenko, and M. Unger [arXiv:2307.06798](#) [astro-ph.HE].
- [109] M.-J. Zhao, X.-J. Bi, and K. Fang *Phys. Rev. D* **107** no. 6, (2023) 063020, [arXiv:2209.03799](#) [astro-ph.HE].
- [110] E. F. Bueno, L. Derome, Y. Génolini, D. Maurin, V. Tatischeff, and M. Vecchi [arXiv:2208.01337](#) [astro-ph.HE].
- [111] D. Maurin, E. F. Bueno, Y. Génolini, L. Derome, and M. Vecchi *Astron. Astrophys.* **668** (2022) A7, [arXiv:2203.00522](#) [astro-ph.HE].
- [112] P. D. L. T. Luque, M. N. Mazziotta, F. Loparco, F. Gargano, and D. Serini *JCAP* **07** (2021) 010, [arXiv:2102.13238](#) [astro-ph.HE].
- [113] M. J. Boschini *et al.* *Astrophys. J. Suppl.* **250** no. 2, (2020) 27, [arXiv:2006.01337](#) [astro-ph.HE].
- [114] N. Weinrich, Y. Génolini, M. Boudaud, L. Derome, and D. Maurin *Astron. Astrophys.* **639** (2020) A131, [arXiv:2002.11406](#) [astro-ph.HE].
- [115] M. Boudaud, Y. Génolini, L. Derome, J. Lavallo, D. Maurin, P. Salati, and P. D. Serpico *Phys. Rev. Res.* **2** no. 2, (2020) 023022, [arXiv:1906.07119](#) [astro-ph.HE].
- [116] C. Evoli, G. Morlino, P. Blasi, and R. Aloisio *Phys. Rev. D* **101** no. 2, (2020) 023013, [arXiv:1910.04113](#) [astro-ph.HE].
- [117] S. P. Wakely *et al.* *PoS ICRC2023* (2023) 118.
- [118] D. Maurin, E. Ferronato Bueno, and L. Derome *Astron. Astrophys.* **667** (2022) A25.
- [119] L. Šerkšnytė *et al.* *Phys. Rev. D* **105** no. 8, (2022) 083021, [arXiv:2201.00925](#) [astro-ph.HE].
- [120] J. Rafelski and B. Muller *Phys.Rev.Lett.* **48** (1982) 1066. [Erratum: *Phys.Rev.Lett.* 56, 2334 (1986)].
- [121] J. Bartke *et al.*, [NA35 Collab.] *Z. Phys. C* **48** (1990) 191–200.
- [122] T. Alber *et al.*, [NA35 Collab.] *Z. Phys. C* **64** (1994) 195–207.
- [123] F. Antinori *et al.*, [WA97 Collab.] *Eur. Phys. J. C* **11** (1999) 79–88.
- [124] F. Antinori *et al.*, [NA57 Collab.] *J. Phys. G* **32** (2006) 427–442, [arXiv:nucl-ex/0601021](#).
- [125] M. A. Stephanov *J. Phys. G* **38** (2011) 124147.
- [126] M. Asakawa and M. Kitazawa *Prog. Part. Nucl. Phys.* **90** (2016) 299–342, [arXiv:1512.05038](#) [nucl-th].
- [127] M. Gazdzicki, M. Gorenstein, and P. Seyboth *Acta Phys. Polon. B* **51** (2020) 1033, [arXiv:2004.02255](#) [hep-ph].

- [128] J. Adamczewski-Musch *et al.*, [HADES Collab.] *Phys. Rev. C* **102** no. 2, (2020) 024914, arXiv:2002.08701 [nucl-ex].
- [129] S. Acharya *et al.*, [ALICE Collab.] *Eur. Phys. J. C* **81** no. 11, (2021) 1012, arXiv:2105.05745 [nucl-ex].
- [130] D. Tlusty, "The RHIC Beam Energy Scan Phase II: Physics and Upgrades," in *13th Conference on the Intersections of Particle and Nuclear Physics*. 10, 2018. arXiv:1810.04767 [nucl-ex].
- [131] M. Maćkowiak-Pawłowska, [NA61/SHINE Collab.] *PoS CPOD2021* (2022) 028, arXiv:2111.05042 [nucl-ex].
- [132] M. S. Abdallah *et al.*, [STAR Collab.] *Phys. Rev. Lett.* **128** no. 20, (2022) 202303, arXiv:2112.00240 [nucl-ex].
- [133] A. Aduszkiewicz *et al.*, [NA61/SHINE Collab.] *Eur. Phys. J. C* **76** no. 11, (2016) 635, arXiv:1510.00163 [hep-ex].
- [134] A. Acharya *et al.*, [NA61/SHINE Collab.] *Eur. Phys. J. C* **81** no. 5, (2021) 384, arXiv:2009.01943 [nucl-ex].